ISSN 0252-1075
Research Report No. RR-090

Contribution from
Indian Institute of Tropical Meteorology

AEROSOL MEASUREMENTS USING LIDAR AND RADIOMETERS AT PUNE DURING INDOEX FIELD PHASES

by

MAHESKUMAR R.S., DEVARA P.C.S., RAJ P.E.,
JAYA RAO Y., PANDITHURAI G., DANI K.K.,
SAHA S.K., SONBAWNE S.M. and TIWARI Y.K.

PUNE – 411 008
INDIA

DECEMBER 2001

CONTENTS

Aerosol Measurements Using Lidar and Radiometers at Pune During INDOEX Field Phases

R.S. Maheskumar, P.C.S. Devara, P. Ernest Raj, Y. Jaya Rao, G. Pandithurai, K.K. Dani, S.K. Saha, S.M. Sonbawne and Y.K. Tiwari

Indian Institute of Tropical Meteorology, Pune 411 008, India

ABSTRACT

In this report, we present the results of special observational programmes relating to atmospheric aerosols organized at the Indian Institute of Tropical Meteorology (IITM), Pune, India during the INDian Ocean EXperiment (INDOEX) field phases. These programmes involve synchronous measurements of aerosol, ozone and precipitable water vapour using ground-based lidar, multi-channel solar radiometer (MSR), high spectral resolution radiometer (HSRR) and MICROTOPS II sunphotometer and ozonometer during the first field phase (FFP) i.e. from 17 February to 31 March 1998 and intensive field phase (IFP) from 1 January to 31 March 1999. Also included in the report are the results of aerosol characterization experiments conducted over the Arabian sea and Indian ocean utilizing the MSR installed onboard ORV Sagar Kanya research vessel. Besides the significant deviations between aerosol features over the land and oceanic regions, the lidar-derived aerosol column content in the boundary layer and radiometer-observed height-integrated aerosol optical depth (AOD) show significant trend and characteristic changes in aerosol size distributions over land during both FFP and IFP. Moreover, the IFP measurements indicate higher aerosol extinction as compared to those of FFP. Besides an increasing trend in total column ozone throughout the IFP, it exhibits opposite variation with those observed in AOD and water vapour over land. Comparison between the boundary layer AODs and total column AODs reveals that the observed increasing trend is not confined to the boundary layer alone but extends to higher altitudes also with significant contribution from the former to the latter. Considering the airmass trajectories, type and residence time of aerosols and prevailing meteorological conditions over the land and oceanic regions during the observational period, the present results indicate a significant forcing due to aerosols and their pre-cursor gases.

1. Background

The Indian Ocean Experiment (INDOEX) is a focused field experiment with international participation from the United States, Europe and India in the equatorial Indian Ocean region (Ramanathan et al., 1998). INDOEX addresses questions of climate change that are of high priority and of great value for the international scientific community. The main goal of this experiment was to study natural and anthropogenic climate forcing by aerosols and feed backs on regional and global climate. With this main objective of assessing climate forcing due to aerosols and trace gases of natural and anthropogenic origin, particularly over the Indian Ocean, an integrated observational programme (INDOEX) has been launched in the country and some pilot experiments have been conducted during 1996 and 1997.

The equatorial Indian Ocean during the northeast monsoon season is a unique natural laboratory for addressing these objectives. The selected experiment area is probably the only place in the world where an intense source of continental aerosols, anthropogenic trace species and their reaction products (e.g., sulfates and ozone) from the northern hemisphere is directly connected to the pristine air of the southern hemisphere by a cross equatorial monsoonal flow into the ITCZ. Furthermore, the deep convection within the ITCZ gives rise to extensive mid- and upper-level cloud systems.

INDOEX has three major scientific objectives:

(i) Assess the significance of sulfates and other continental aerosols for global radiative forcing;
(ii) Assess the magnitude of the solar absorption at the surface and in the troposphere including the Intertropical Convergence Zone (ITCZ) cloud systems; and
(iii) Assess the role of the ITCZ in the transport of trace species and pollutants and their resulting radiative forcing.

The first objective will contribute to a better understanding of the decadal and longer time scale forcing; the second will lead to improved coupled ocean-atmosphere models; and the third will aid in the development of tropospheric chemistry models.

In order to assess the climate forcing due to aerosols and trace gases of natural origin and anthropogenic origin, particularly over the tropical Indian Ocean, the FFP98 of the INDOEX, involving several coordinated scientific experiments from different platforms (ground-based, ship-borne, airborne and satellite-borne), were conducted by the scientists from India, USA and Europe (Mitra, 1999). Some interesting results obtained from the Indian experiments have already been published in a special section of the Journal "Current Science" in 1999. By following the experience and outcome of the FFP, the IFP of this multi-institutional, international scientific experimental program has been organized from the middle of winter 1998/99 till the beginning of pre-monsoon 1999.

Besides some measurements of aerosols over the Arabian Sea and Indian Ocean from the Sagar Kanya cruise, and trace gases over an island station (Mauritius), a variety of land-based experiments involving direct and remote sensing measurements of aerosols and trace gases have been conducted at the IITM, Pune, as part of the INDOEX-IFP99. Atmospheric aerosols over this land site associated with urban environment exhibit unique features during winter months (December, January and February) due to frequent low-level inversion caused haze formation and poor visibility (Devara et al., 1999a). Rapid fall in daily temperature, light surface winds, low relative humidity and incursion of aerosol particles and precursor gases due to combustion processes during these months make the study of aerosols more

important from the point of view of their generation, growth and transport processes. Such studies over the ground sites like Pune where low-level winds are predominantly from the north-east direction and the air mass, rich in nuclei of continental origin, passes over the station from the November month onwards, will provide an insight into the transport of aerosols and precursor gases from continents to pristine Ocean surface. Observations of aerosols / pre-cursor gas distributions over the land in conjunction with those over the Oceanic regions are essential and greatly help in understanding the nature and extent of mixing continental polluted air with the pristine maritime air. By keeping this aspect in view a variety of land based experiments involving direct and remote sensing measurements of aerosol and trace gases have been conducted at the Indian Institute of Tropical Meteorology (IITM), Pune during the first field phase (FFP 98) and intensive field phase (IFP 99). In addition, IITM has carried out measurements of aerosols over the Arabian Sea and Indian Ocean on board ORV Sagar Kanya, and trace gases over an island station (Mauritius) during the IFP 99. The present research report is a contribution towards the results obtained from the IITM lidar and radiometers during FFP 98 and IFP 99. The details of the observational site characteristics, equipment used, data and analysis techniques and salient results obtained from the above instruments are also presented in this report.

2. Experimental sites

2.1 Land site (Pune)

The experimental station, Pune (18°32'N, 73°51'E, 559 m AMSL) is situated on the lee side of the Western Ghats and is about 100 km inland from the west coast of India. The experimental site is located at an elevation of 570 m AMSL and is surrounded by hillocks as high as 760 m AMSL (valley-like). The environment in the immediate vicinity of the station is urban, with several small industries nearby. Also, the stone quarries (east side) and brick kilns (west side) at a distance of about 1 km aerial distance from the experimental site, are the major local anthropogenic sources, contributing to the aerosol loading at the site. In addition, there is major urban activity to the east of the site; to the west is a sparsely populated area. Soil-dust is the major source of aerosols present over the experimental station. Formation of aerosols in the accumulation mode is considered to be due to gas-to-particle conversion processes, whereas the coarse aerosols are attributed mainly to wind-blown dust. The possible aerosol type present over the station is a mixture of water-soluble, dust-like and soot-like aerosols. The transport and dispersion of pollutants, particularly those in the lower levels of the atmosphere, are believed to be affected by the circulation processes associated with this type of terrain.

2.1.1 Meteorology

The weather at the experimental site during the pre-monsoon (March-May) season is very hot with the daytime maximum temperature reaching around 40°C and surface winds are mostly gusty. During this season the dust content in the atmosphere is at a maximum. Cumulonimbus type cloud development takes place around late afternoon to evening. Development of low due to increased heating over land starts over India in pre-monsoon when the whole country has a flat pressure distribution with slightly higher pressures over the Arabian Sea and Bay of Bengal. Heating over land is more prominent to the north of 20° N and the axis of the low is at a more northerly latitude over India. Over Peninsula a trough forms with the axis along longitude 78° E. In March (pre-monsoon) over land, north of 17° N, winds are from west and south of it from east. Anti-cyclonic wind circulations have developed with centers at 18° N and 60° E in the Arabian Sea and 16° N and 90° E in the Bay of Bengal.

Winds are predominantly westerly during the summer monsoon (June - September) season which brings a large influx of moist air from the Arabian Sea. The region receives light intermittent or continuous rain from cumulus and stratocumulus clouds under the influence of large-scale convergence due to synoptic systems, and the atmosphere is relatively free from dust during this season.

The westerly flow weakens in the lower troposphere and the easterly flow sets in during the post-monsoon (October and November) season. In post-monsoon the trough over northern India shifts to the Bay of Bengal with the trough line along 13°N and the pressure field is flat over the country. Also, winds are very much variable over the country as a whole, in association with flat pressure distribution. In the Arabian Sea winds are mainly westerly south of 8°N, and northerly between 8°N and 18°N, changing to westerlies in the north of Arabian Sea. There is an anti-clockwise circulation of wind with center at about 17°N, 60°E. In the Bay, winds are mainly west-south-west to the south of the trough line along 13°N and about south easterly to the north of it. The daily minimum temperature falls very rapidly by the end of October and continental airmasses rich in nuclei of continental origin pass over the region during this season.

Fair weather conditions with clear skies and very low relative humidity exist during the winter (December - February) Season. The daily surface minimum temperatures go down to 3-4°C and light surface winds prevail in this season. Low-level inversions during the morning and evening hours, and dust haze during the morning hours, occur during this season. Also, inversion of dry polar continental air in the wake of low pressure systems (western disturbances) moving across the far north-western parts of the country takes place during this season.

2.2 Ocean site (Arabian Sea & Indian Ocean)

Advection of continental aerosols over Oceanic environment in the tropical region can cause large-scale climate perturbations (Charlson et al., 1992) particularly due to the presence of ITCZ which mixes the polluted northern hemispheric air mass with the pristine southern hemispheric air mass vigorously. Therefore, observations of aerosol distributions over the land in conjunction with those over the oceanic regions are essential and such observations will greatly help in understanding the nature and extent of mixing of continental polluted air with pristine maritime air.

2.2.1 Synoptic features

The circulation patterns over Arabian Sea and Indian Ocean during the different months of the year. During January north-east winds prevail over the whole of Arabian Sea whose strength is about 20 knots. The equatorial belt experiences very weak winds of 5 to 10 knots. The mean monthly pressure varies from 1011 mb to 1018 mb, increasing towards north. North of 15°N winds are very weak and varying direction but the north-east winds maintain their direction with reduced strength in southern part of Arabian Sea during the month of February. The anticyclonic cell located above 22 ½°N moves southward which shifts the isobars towards the equator. The anticyclonic cell moves south-westerly and there is a marked change in the wind strength and direction during March. Most of the time the winds are very weak, about 10-15 knots. Near the west coast of India, northerly and north-westerly winds prevail. During April the atmospheric pressure variation is very irregular. Also the wind blow in very much varying directions with their weak strength of about 5 knots. This month is transition period from north east winds to south west monsoon winds. There is continuous anticlock wise swing in the direction of winds over the Sea. The atmospheric pressure distribution in May is much more regular when compared to April and

hence the wind direction is also fairly regular. The winds are westerly up to 20°N with strength up to 5-10 knots. The south west monsoon conditions begun in the month of May, now fully establish and the Arabian Sea as well as peninsular India are fully under the south west monsoon winds. The south west winds are much stronger, reaching as much as 30 knots. The winds are generally south westerly but near the west coast they are very nearly westerly and have lesser speed of 15-20 knots. This is due to the increased land friction and obstruction due to western ghats. The pressure distribution is uniform. The south west monsoon is at its peak during July and there is no much difference in the meteorological conditions when compared to June. During August also south west monsoon continues to be active with no change in the meteorological conditions. Many high pressure centres and depression form near the equator. The withdrawal of south west monsoon begins in September and there is a distinct change in the atmospheric condition. Like April October month is also a period of transition and now the change is from south west monsoon to north east monsoon. Low wind velocities, continuously changing direction and the presence of many depressions and highs. The northeast monsoon fully establishes over the Indian subcontinent. In December, the north east monsoon further strengthens over the north Indian Ocean and north east winds of 15 to 20 knots are very common.

As a part of the INDOEX field phase campaigns, the aerosol measurements were also undertaken over oceans by deploying the measuring instruments onboard research vessel Sagar Kanya. Scientists from various countries and research institutions have participated with their instruments to meet the objectives of the campaign. There were two different cruises for the two phases, FFP and IFP. From IITM also there were participants during both the cruises. The multi-channel solar radiometer observations were carried out onboard ORV Sagar Kanya research vessel during the INDOEX IFP.

3. Instrumentation

The continuous wave bistatic Argon ion lidar and solar radiometers have been extensively used to collect the aerosol information during both the INDOEX field phases. A brief description of these instruments are given in the sections to follow.

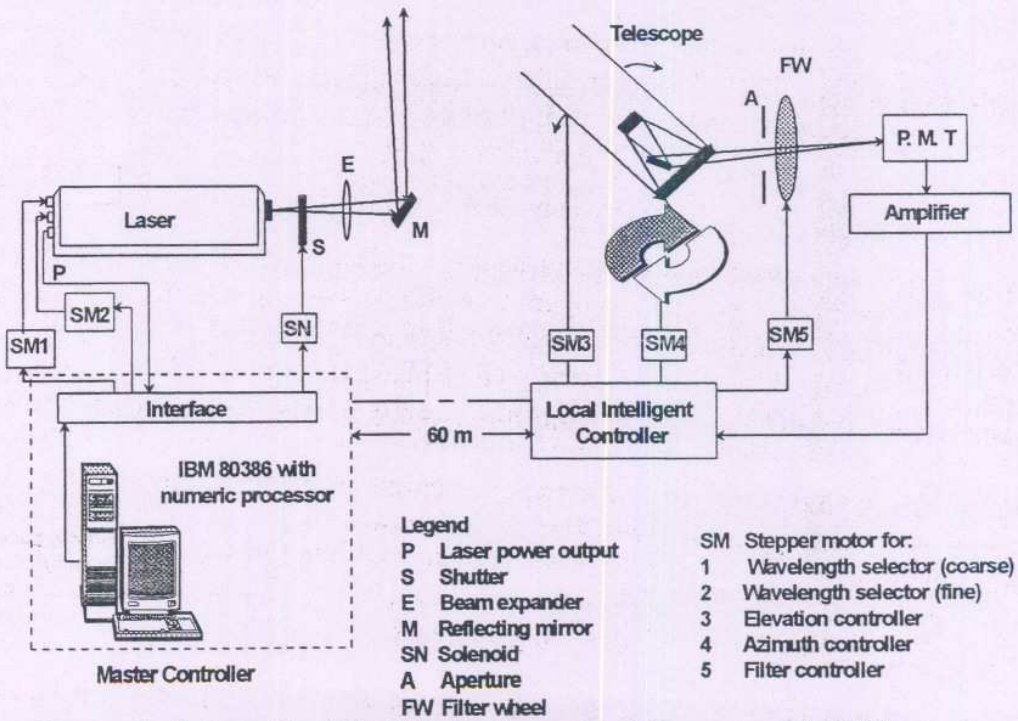

Figure 1 : Schematic of the bistatic Argon ion lidar system at IITM

3.1 Bistatic Argon ion lidar

A bistatic lidar system (Figure 1) has been in continuous operation here in Pune since October 1986 (Devara and Ernest Raj, 1987) where the transmitter and receiver are separated by a distance of about 60 m in the horizontal plane. The transmitter part of the lidar system consists of a continuous wave (CW), tunable Argon-ion laser operating at the wavelength of 514.5 nm and a beam steering device to tilt the beam in the horizontal and vertical plane. The receiving system essentially consists of a 25-cm diameter Newtonian telescope, narrow-band interference filter of 1 nm FWHM, a Peltier cooled photomultiplier tube and intermediate optics. The receiving system also consists of an aperture of diameter adjustable from 2 to

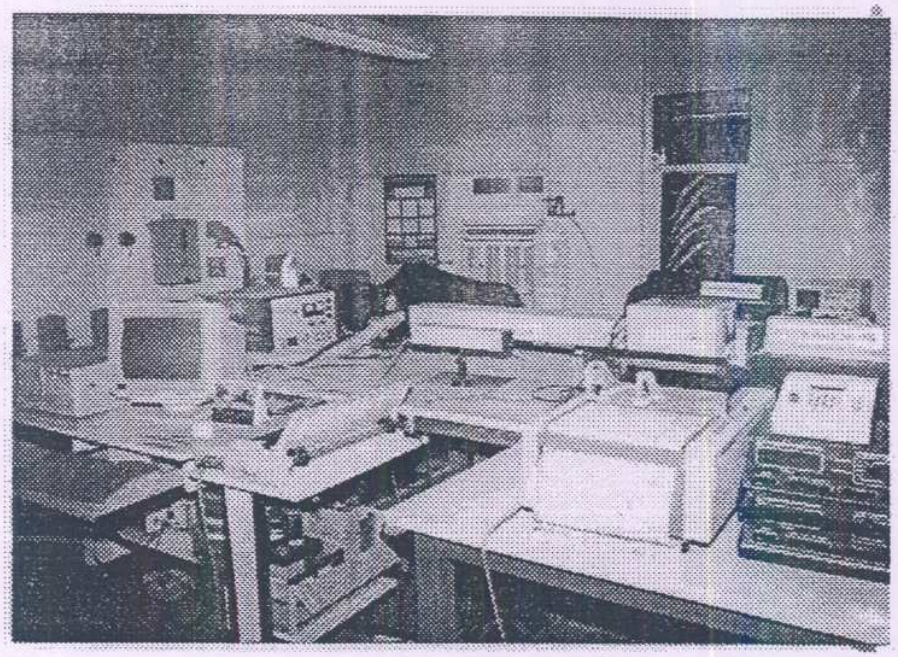

Figure 2 : Photograph of the laser lab at IITM with different laser systems

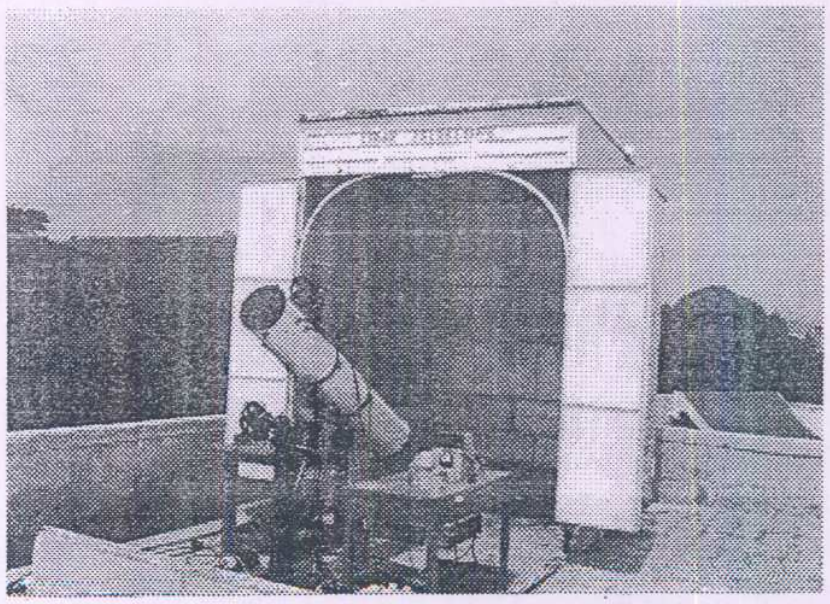

Figure 3 : Newtonian telescope - Receiver part of the lidar system

25 mm. Figure 2 & 3 shows the bistatic lidar system available at IITM, Pune. The vertically transmitted laser beam is scanned by the receiver at pre-selected elevation angles which correspond to different altitudes from 50 m to 6800 m at different height intervals. Thus, altitude profile of scattered signal strengths are obtained for further analysis. The entire lidar

Table 1. Main characteristics of the computer-controlled bistatic lidar system at IITM, Pune

Transmitter		
Laser	Lexel Model 95-4, tunable, continuous wave Argon ion	
Wavelengths	0.5145, 0.4965, 0.4880, 0.4765 μm	
Output power	4 W (multiline)	
Beam divergence	0.283×10^{-6} ster.	
Beam diameter (at $1/e^2$ points)	1.3 mm	
Polarization	linear	
Receiver		
Telescope	250 mm dia, F/7.6, Newtonian reflector (astronomical quality)	
Focal length	190 cm	
divergence	1.36×10^{-6} ster.	
Detector	RCA C31034A	
Photomultiplier tube (PMT)		
PMT gain	$\geq 10^6$	
Cathode efficiency	119 mA/W	
PMT cooler	PFR TE 206 TSRF	
housing	0.001 μm FWHM filter equipped Peltier-cooled RCA C31034A photomultiplier	
Detector		
Filter bandwidth	0.001 μm	
Type of signal processing	Digital	
	Master controller	**Local intelligent controller**
Processor (CPU)	80386 operating at 33 MHz with 80387 numeric maths co-processor	
Mass storage	2 floppy disc Drives 1.2 & 1.4 MB, hard disc 40 MB	
Analog-to-Digital conversion	10 μs	10 μs
Accuracy	13 bit (including sign)	13 bit (including sign)
Interface	One parallel port (Centronics) and one serial port (RS 232-C)	8255 with 24 I/O lines and PC compatible
Data transfer	Polling or interrupt (selectable)	Polling or interrupt (Selectable)
Programmable gain amplifier	LM 356 with gain selection through software	LM 356 with gain selection through software
Real-time display	12" EGA colour monitor	
Printer	DOT Matrix 132 column / 240 CPS	
Plotting format	Raw signal strength as a function of altitude	

system is controlled by a PC-based on-line control and data acquisition system for real-time monitoring (Devara et al., 1995). The details of the lidar system, its main characteristics and the method of extraction of aerosol vertical distributions from lidar return signals can be found in earlier publications (Devara and Ernest Raj, 1989; 1993, Ernest Raj and Devara, 1989). The main specifications of the lidar system used in this study are given in Table 1. The lidar has been operated on 25 days during FFP 98 and on 50 days during IFP 99 coinciding with other observations at the experimental site and also with the cruise measurements. The observations were carried out during post-sunset period, around 1900 hr. on each experimental day.

3.2 Multi-channel solar radiometer

The multi-channel radiometer (MSR) (Figure 4) used in the present study composed of fourteen narrow-band (2-5 nm FWHM) interference filters with their peak transmission at 317, 335, 354, 371, 382, 385, 400, 502, 600, 778, 940, 1060, 1190 and 1630 nm. The instrument is equipped with an altazimuth arrangement to track the Sun's disc precisely. The Barium Selenide photocell detects the quasi-monochromatic solar irradiance at the above

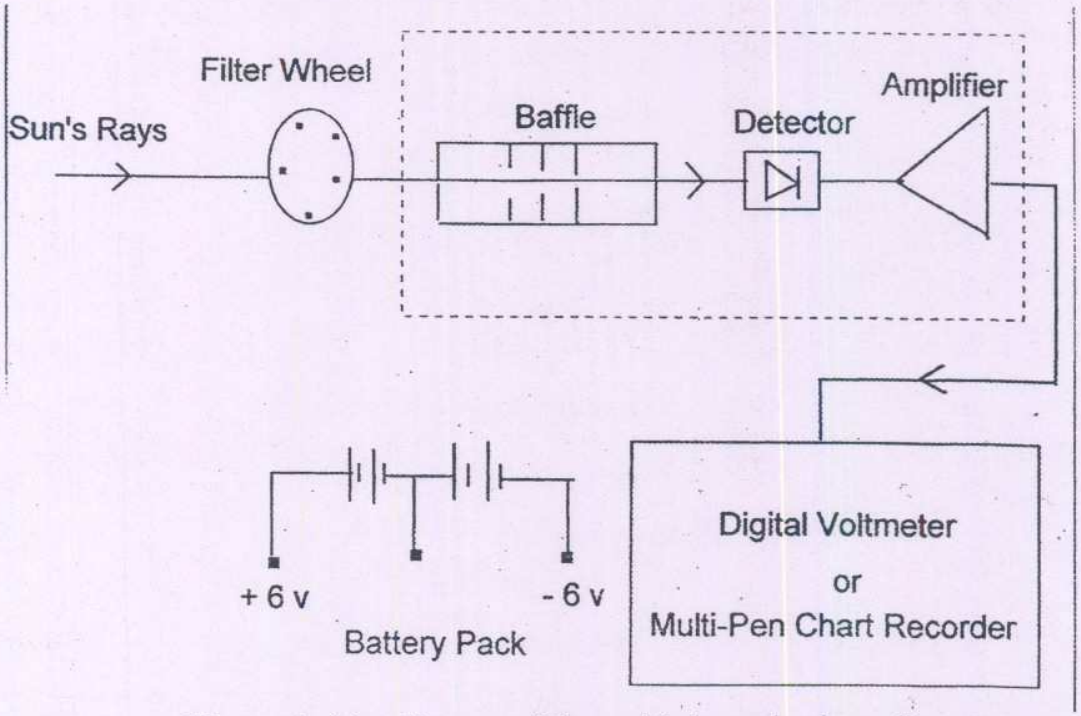

Figure 4 : Line diagram of the multi-channel solar radiometer

mentioned wavelengths, and a Nexus Model 201 Operational Amplifier records the data. The field-of-view of the radiometer is kept at less than 3 degrees so as to eliminate the contamination due to stray light. The complete sunphotometer was mounted on a wooden platform which is attached to a tripod for its easy steerability. The instrument has been operated from the terrace of the Institute's building in order to make it free from nearby tall topographic objects and thereby to bring the solar radiation into the radiometer at a wide range of solar elevation angles. The main features of the instrument is depicted in Figure 5.

The observations were made from morning till evening on the days when the sky was nearly free of visible clouds, and none were near the line-of-sight to the Sun. The observations were repeated at an interval of about 10 minutes when the airmass changes rapidly during the post-sunrise and pre-sunset periods. Data obtained with each filter were corrected for background noise by off-setting the detector output to zero by completely

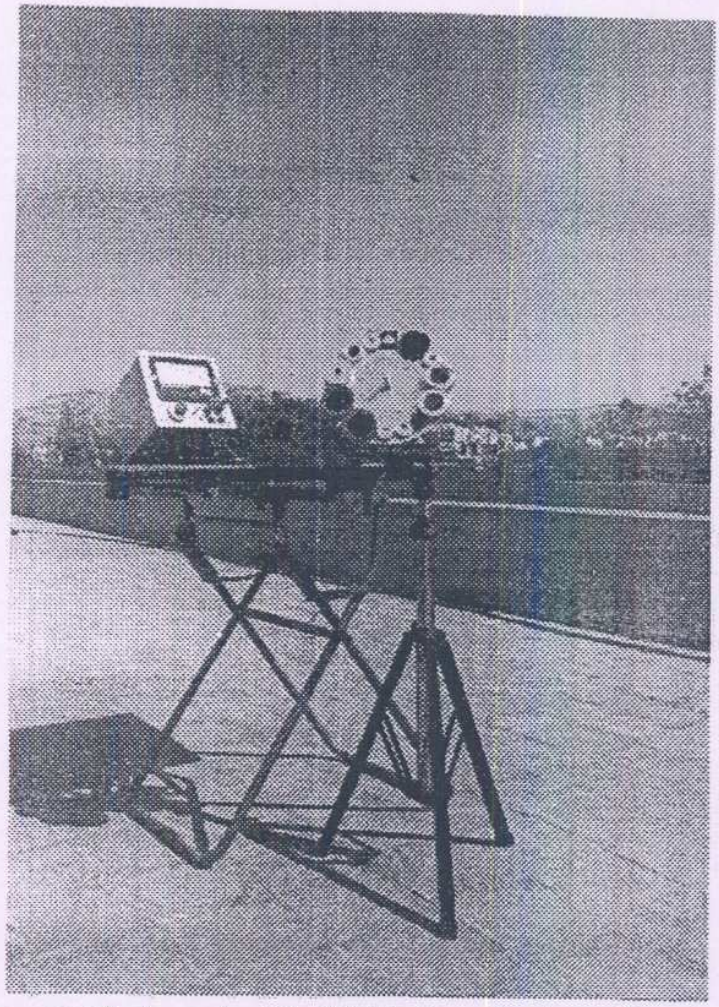

Figure 5 : Photograph of the Multi-channel solar radiometer

covering the filter before it is exposed to the Sun. This procedure is repeated for all the data sets recorded for different solar zenith angles.

3.3 High spectral resolution radiometer

The high spectral resolution radiometer (HSRR) used in the present study is displayed in Figure 6. It composed of a SPEX model 1680B double monochromator equipped with holographic gratings (1800 grooves / mm), a Peltier-cooled photomultiplier tube (PMT), an on-line data acquisition / processing system and an automatic Sun tracker to bring the solar radiation into the entrance slit of the HSRR. After passing through the monochromator, the radiation is focused onto an EMI Model 9659 QB, S-20 cathode PMT. The output of the PMT is passed through a discriminator to enhance the signal-to-noise ratio and further amplified by a low-noise, variable gain FET input amplifier. The amplified signal is digitized using a 12-bit analog-to-digital converter Model 7880. The data are acquired by a mini-computer. Figure 7 portrays the complete HSRR used for the measurements. The system has been installed on the terrace of the Institutes' building which is about 12 m high above the ground level, in order to avoid the obstructions due to surrounding tall topographic objects while tracking the Sun. In order to remove the background noise from the observed spectrum, noise and signal plus noise values were recorded separately and the average value of the background noise was subtracted from each value of the signal plus noise spectrum to get the

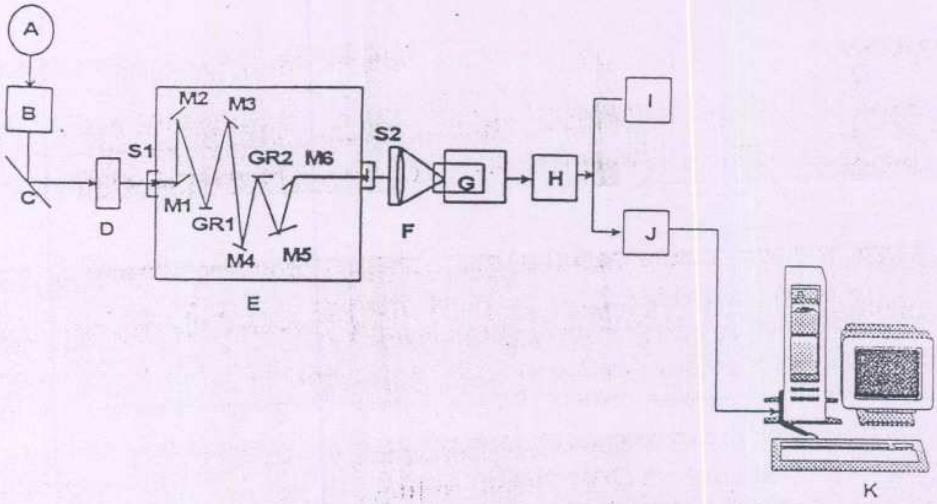

A : Source (Sun or Moon)
B : Heliostat or Sun (Moon tracker)
C : Reflecting mirror
D : Shutter
E : Double monochromator
S_1 : Entrance slit; S_2 : Exit slit;
M_3 & M_5 : Collimating mirrors;
F : Condensing lens
G : Photomultipler with cooler housing
H : Amplifier (analog or photon counting)
I : Multipen chart recorder
J : Interface
K : Data acquisition, analysing and plotting system
M_1, M_2, M_4, M_6 : Reflecting mirrors
GR_1 & GR_2 : Holographic gratings

Figure 6 : Optical-electrical layout of the HSRR used in the present study

signal spectrum. The HSRR was allowed to scan the solar irradiance in the 0.4 - 0.72 μm wavelength region at a rate of 0.005 μm /s. A detailed description of the HSRR, its calibration and data retrieval procedures and inter-comparison with sunphotometer have been published elsewhere (Devara et al., 1995).

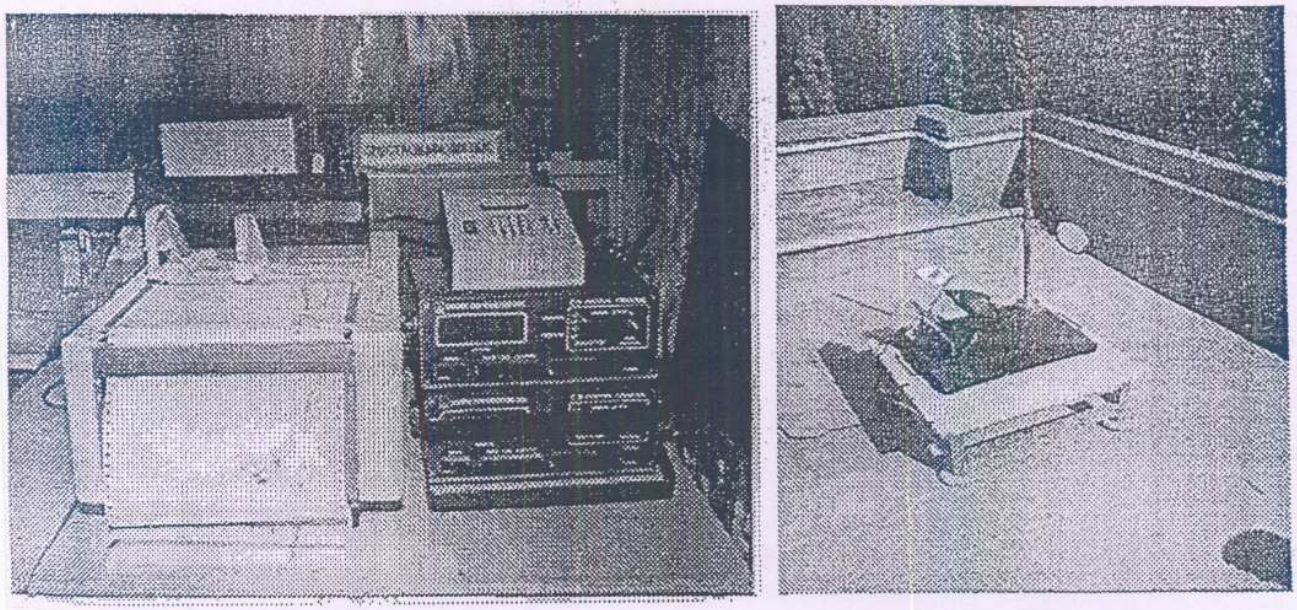

Figure 7 : Photograph showing the HSRR with sun-tracker

3.4 Microtops sunphotometer and ozonometer

Two compact, on-line, multi-band solar radiometers, (MICROTOPS-II, manufactured by M/s Solar Light Co., USA) has been used in the present experiment. Figure 8 shows

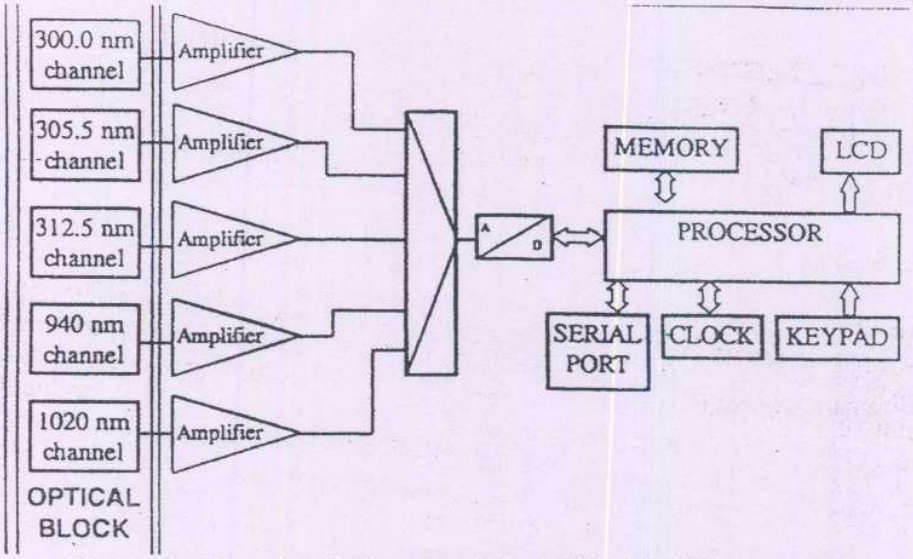

Figure 8 : Functional diagram of the MICROTOPS ozonometer

functional diagram of these hand-held radiometers. These instruments yield instantaneous estimates of aerosol and gaseous optical depths as opposed to conventional ones. One of these radiometers (sunphotometer) provides height-integrated AOD (or extinction) at six wavelengths covering from UV to NIR and hence the size distribution of aerosols, and the other radiometer (ozone and water content monitor) determines total column ozone (using the UV band) and precipitable water content (using the NIR band) simultaneously. Both the

Figure 9 : Photograph of the MICROTOPS sunphotometer and ozonometer

radiometers are mounted on a single wooden platform which is in-turn fixed to a tripod for achieving high stability, time synchronization between observations and easy focusing of radiometers to the Sun's disk. A photograph depicting the front view of the radiometers is shown in Figure 9. Each radiometer is equipped with internal barometer/altimeter for monitoring of atmospheric pressure and altitude of the experimental location. The global positioning system (GPS) receiver provides the geographical coordinates of the site, which are used for estimating the local air mass.

The LCD on sunphotometer provides instantaneous display of AOD, record number and several other information like power density etc. recorded at each wavelength. Similarly, the LCD on ozone and water content monitor provides instantaneous display of total column ozone and water content together with other parameters such as received solar power density at each filter. Moreover, these radiometers are equipped with built-in algorithms for computing the ozone, water content and AOD from the output of the amplifier recorded for each filter. The radiometers are operated initially by keeping the cover closed for the optical blocks (consisting of windows, filters etc.). During this period, the instrument stores the background values for all the filters. In the next few seconds, on removing the cover, it collects a set of over 25 observations for each filter. The average value, thus obtained for each filter, is used to compute the spectral variation of columnar AOD, ozone and water content instantaneously, and are depicted on the display for a quick look, and stored in the

Table 2 : Main specifications of the three radiometers used

Specification	**Spectroradiometer**	**Multi- Channel Solar radiometer**	**MICROTOPS II**
Source	Sun or Moon	Sun	Sun
Spectral range	200nm - 700nm (continuous)	313nm - 1630nm (discrete)	300nm – 1020nm (discrete)
Spectrum analysis	Double monochromator equipped with holographic gratings (1800 grooves/mm)	Narrow-band interference filters (2nm-5nm FWHM)	Narrow-band interference filters (5nm -10nm FWHM)
Field of view	$1^0 \times 3^0$	$< 3^0$	2.5^0
Detector	EMI model 9659 QB Photomultiplier tube	Barium Solenoid Photocell	GaP Photodiode
Amplifier	EMI CD 100 Photon counter	Nexus model 201 Operational amplifier	FET-input Operational amplifier
Data acquisition	12 bit analog device A/D converter	Manual/ Multi Pen chart	20 bit resolution A/D converter
Scan speed	Scan speed 0.01 units/sec	For one filter scan with in 30sec.	All filter scan with in 10 sec.
Scanning method	Continues	Serially	Parallel
Data Analysis	Offline	Offline	Online
Recording Format	Optical depth versus solar zenith angle (air mass)	Optical depth versus solar zenith angle (air mass)	Optical depth versus solar zenith angle (air mass)
Display	On PC	Analog meter Moving coil type 1ma, 41	On LCD 3 & 1/2 digits

memory. Apart from constant monitoring of $F_0(\lambda)$ which serves as calibration constant for each channel, inter-instrumental comparison of AOD at either exact or near-synchronous wavelengths of all-the-time near-simultaneously operated multi-channel solar radiometer and HSRR has been carried out periodically to ensure the stability and reliability of AODs, ozone and water content measured using the MICROTOPS radiometers. As these radiometers have been installed during May 1998, the results obtained from the data collected during the INDOEX-IFP period only will be discussed.

The main specifications of the above three radiometers are compared in Table 2.

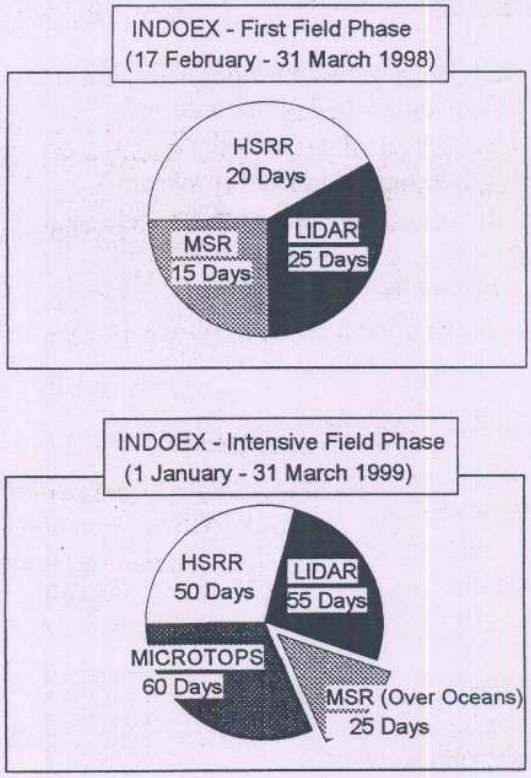

Figure 10 : Observational details during FFP 98 and IFP 99

4. Database and method of analysis

Figure 10 depicts the observational details of various instruments operated during the INDOEX FFP and IFP. During the period of INDOEX-FFP (from 17 February to 31 March 1998) all the three instruments have been operated on about 25 days. But during INDOEX-IFP which spread over a period of three months (from 1 January to 31 March 1999), lidar was operated on about 40 days and HSRR observations were carried out on about 45 days. The sunphotometer was operated on board ORV Sagar Kanya cruise # 140 and hence the data pertains to the Ocean environment. Before the deployment of the MSR, it has been thoroughly calibrated against similar equipment under an inter-comparison campaign conducted at SPL, VSSC, Thiruvananthapuram during January 1-7, 1998.

4.1 Aerosol number density and boundary layer parameters

A brief discussion on the lidar equation for the bistatic case is presented here. Let the transmitting power of continuous wave laser be P_T and V the volume enclosed by the intersection of the transmitting and receiving beams (scattering volume). Let the range of

the center of the scattering volume V be R_1 and R_2 from the transmitter and receiver, respectively. Let T_X and T_R be the atmospheric transmittances along R_1 and R_2, respectively, and $d\omega_1$ the transmitted beam solid angle. The intensity of the transmitted beam at R_1 is,

$$\frac{P_T T_X}{R_1^2 d\omega_1} \qquad [1]$$

and the scattered intensity received at the ground by the receiver is

$$\frac{P_T T_X V}{R_1^2 d\omega_1 R_2^2} T_R [N\sigma(\theta)] \qquad [2]$$

Where N is the number density (cm^{-3}) of the scatterers and $\sigma(\theta)$ is the differential scattering cross section ($cm^2\ sr^{-1}$) at scattering angle θ. If A_R is the collecting area of the receiver and η is the system constant including overall optical efficiencies of the transmitter and receiver optical systems, the received power P_R is then given by

$$P_R = \frac{P_T T_X T_R V A_R \eta [N\sigma(\theta)]}{R_1^2 R_2^2 d\omega_1} \qquad [3]$$

The received power P_R can be estimated from the photomultiplier anode current knowing the gain and cathode efficiency. The scattering volume V can be estimated from the geometry of the bistatic setup. The atmospheric transmittance T ($T_X T_R$), can be calculated using the optical depth (τ) measured for different scattering angles. Once all the parameters in the above equation are known, aerosol number density can be reckoned at different scattering angles, that is at different altitudes. The aerosol number density profile obtained after every experiment has been integrated up to an altitude of 1100 m to get aerosol columnar content, which gives a picture of aerosol loading in the atmospheric boundary layer. It can be given in the form of a mathematical expression as

$$\sum_{i=50}^{1100} \left[\frac{C_i + C_{i+1}}{2} \right] (h_{i+1} - h_i) \ \ cm^{-2} \qquad [4]$$

where C_i and C_{i+1} are the aerosol concentration at the altitudes h_i and h_{i+1}, respectively.

Since the lidars, through light scattering, detect the aerosol distribution itself within the atmospheric structure, and changes in backscatter with time and space yield information on transport and diffusion processes, they are very useful for determining the height to which pollution originating in the mixed layer has been carried. One way of determining these heights from the lidar-derived aerosol concentration profiles is through the computation of normalized concentration gradient (NCG). The normalized concentration gradients (NCGs) were computed from the vertical profiles of aerosol number density gradients normalized by the local aerosol number density using the following formula suggested by Sasano et.al. (1982) as,

$$NCG(Zi) = \left[\frac{[C_{(Zi+1)} - C_{(Zi-1)}]}{(Z_{i+1} - Z_{i-1}) C_{(Zi)}} \right] 100 \qquad [5]$$

where C_i is aerosol concentration at the height Z_i. The normalization procedure followed here eliminates the variability in the lidar system efficiency and in the aerosol concentration, and portrays the altitude structure of the aerosol layers.

As suggested by Endlich et al. (1979), the largest negative gradient nearest to the surface in the lidar backscatter or the aerosol concentration is associated with the sharpest decline from high to low particulate concentrations and, marks the mixing depth. This method of marking the mixing depth has been widely used to study the evolution of the

daytime mixed layer, which extends most of the time, beyond 1 km. The night-time mixed-layer heights extending up to 1500 m during the post-sunset period in fine weather have also been reported by some researchers (Sasano et al., 1983). The positive gradients that often occur above the mixing depth denote the aerosol layer structure (stable layers) associated with atmospheric stability.

The ventilation coefficients which indicate the air pollution potential or air quality over a place have been computed using the mixed layer heights and the mean wind speed through the mixed layer. The wind speed data have been obtained from the India Meteorological Department's pilot balloon-theodolight experiments conducted near-simultaneous to the lidar observations.

4.2 Aerosol optical depth and size distribution

Total optical depths were estimated at all wavelengths by applying the computerized linear regression algorithm to the plot between natural logarithm of radiometer output voltage and airmass values (Langley plot). The aerosol optical depth, τ_a in a vertical air column at wavelength λ was determined from the Beer-Bouguer-Lambert law, expressing attenuation of direct solar beam in the atmosphere, in the form

$$F(\lambda) = F_o(\lambda) \exp\left[-m\left\{\tau_R(\lambda) + \tau_g(\lambda) + \tau_a(\lambda)\right\}\right] \qquad [6]$$

where $F(\lambda)$ is the monochromatic solar irradiance reaching the instrument detector, $F_o(\lambda)$ is the irradiance incident on the top of the atmosphere, m is optical airmass, $\tau_R(\lambda)$, $\tau_g(\lambda)$ and $\tau_a(\lambda)$ are Rayleigh, gaseous and aerosol optical depths, respectively. The atmospheric total optical depths have been estimated by means of Langley method. The slope of the regression line gives the total optical depth. Eventhough the measurements are made on clear sky days, errors may be expected due to misalignment of receiver optics. Some times, high output due to invisible (but optically visible) thin cirrus clouds also may give rise to abrupt / spurious values. Such data points were detected and removed from the raw data to avoid improper weights to the derived optical depth and to reduce the scatter in the Langley plot. This has been done by applying statistical student's t-test. Molecular optical depth, was computed by using the expression of Teillet (1990). Since ozone has significant absorption in the Chappuis band (400-650 nm) ozone optical depths at the wavelengths lie in this spectral band were estimated by the method suggested by Kneizys et al. (1980). From the total optical depths, aerosol optical depth (AOD) is obtained by subtracting the contributions due to molecular scattering and ozone absorption. The methodology used to obtain aerosol optical depth from the total optical depth has been explained by many investigators.

The column-integrated aerosol size distributions (ASD) were inverted from spectral variation of aerosol optical depth by following the constraint linear inversion scheme of King et al. (1978) which involves the following Fredholm integral,

$$\tau(\lambda) = \int_0^\infty Q_{ext}(r, \lambda, m)\pi r^2 n_c(r) dr \qquad [7]$$

where r is the particle radius, m is the complex refractive index of aerosol particles, $Q_{ext}(r, \lambda, m)$ is the Mie extinction efficiency parameter, $n_c(r)$ is the columnar aerosol size distribution (i.e. the number of particles per unit area per unit radius interval in a vertical column through the atmosphere). Since n(r) cannot be written analytically, a numerical approach is followed to separate $n_c(r)$ into two parts as $n_c(r) = h(r).f(r)$, where h(r) is rapidly varying function with r and f(r) is slowly varying. Hence the above equation changes to

$$\tau_a(\lambda) = \sum_{j=1}^{q} \int_{r_j}^{r_{j+1}} \pi \; r^2 Q_{ext}(r,\lambda,m) \; h(r) \; f(r) \; dr \qquad [8]$$

In the above equation, the quadrature error will be less if f(r) is assumed to be constant. In that case, a system of linear equations results, which may be written as

$$\tau_a(\lambda) = A\, f(r) + \varepsilon \qquad [9]$$

$$\text{where} \quad A = \int \pi r^2 Q_{ext}(r,\lambda,m) h(r) dr$$

and ε is an error which arises due to deviation between the measured τ_a and theoretical τ_a ($= \Sigma A_{ij} f_i$). Initially, Junge exponent (ν) is computed from the wavelength dependence of AOD and used as zero-order weighting function $h^0(r)$. By using $h^0(r)$ as an initial guess, first order $f^{(1)}$ values are evaluated using the equation

$$f^{(1)} = (A^T S_\varepsilon^{-1} A + \gamma \; H)^{-1} \; A^T \; S_\varepsilon^{-1} \tau_a \qquad [10]$$

Where γ is non-negative Lagrangian multiplier and S_ε is the measured covariance matrix, H is a mean diagonal matrix and superscript T denotes matrix transposition. This iteration procedure is repeated till the observed τ_a comes closer to the re-computed τ_a More detailed discussion on the retrieval of aerosol size distribution is available elsewhere (Maheskumar , 1999).

5. Results and discussion

The main features of the aerosol parameters obtained by operating the bistatic lidar and radiometers during the FFP and IFP are discussed in this section. The results relating to the observations made in each phase and comparison of the common parameters in both phases have been presented below.

5.1 First field phase (FFP)

5.1.1 Vertical distributions of aerosol number density

The observations in the first field phase of the INDOEX campaign were conducted during the period from February 17 to March 31, 1998. The Argon ion lidar at IITM has been operated to retrieve the vertical profiles of aerosol number density. A total of about 25 days of observations are available during this phase. Besides the altitude structures of aerosol concentration, the NBL parameters such as mixing depth, stable layer height and ventilation coefficients have also been derived from the aerosol profiles.

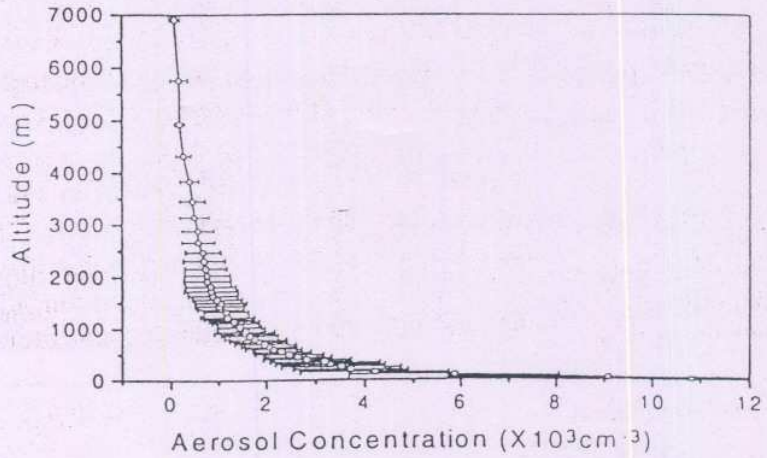

Figure 11 : Mean aerosol number density profile obtained during FFP 98

The aerosol number density profiles obtained with the lidar up to 6.8 km of the atmosphere during night-time during the entire FFP period have been averaged and the mean aerosol number density profile thus obtained is shown in Figure 11. The deviations in aerosol concentration from the mean concentration at each altitude of measurements are depicted with horizontal lines in the figure. The two striking features that can be seen from these profile are (i) rapid decrease of aerosol number density up to about 150 m and thereafter exponential decay with increase in altitude; and (ii) stratified, fine-scale layer structures above the NBL. The first feature is a regular phenomenon seen in almost all the profiles of aerosol number density at this experimental site because of the effect of terrain, while the second one is mainly due to stratified turbulence resulting from wind sheer (Devara and Ernest Raj., 1991).

Aerosols which are lifted during day-time due to convective activity would be suspended for a long time in the lowest layers of the atmosphere, and those emitted near the surface would be confined to lower levels during night-time. As the convective activity decreases, radiative cooling at the surface induces stable stratification near the ground, and sometimes far above the NBL, and advection becomes important in determining aerosol concentration aloft (Devara et al., 1999). Formation of aerosol layers in the atmosphere results in either heating or cooling of the combined earth-atmosphere system depending upon the fraction of the incident solar radiation backscattered and absorbed by the aerosol layer. Thus aerosol layer affect the human life directly and the weather and climate indirectly on different time scales. In order to study such events normalized concentration gradient

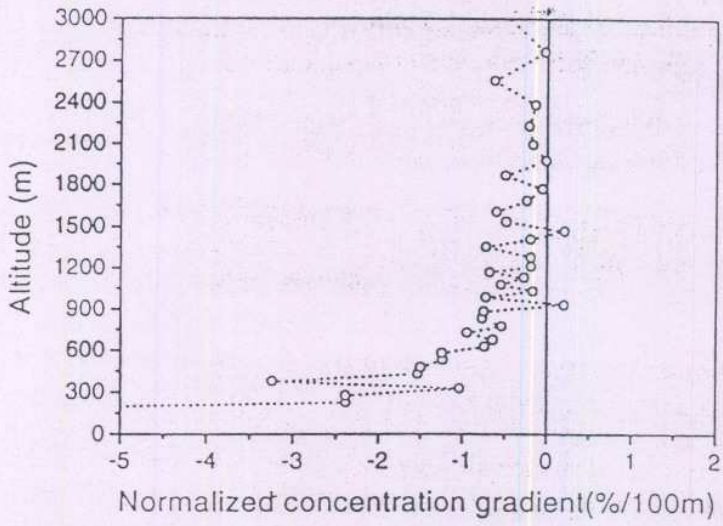

Figure 12 : Mean NCG profile obtained during FFP 98

gradient (NCG) profiles have been derived from the aerosol number density profiles and a mean NCG profile for the FFP period is shown in Figure 12. As explained above the mixed layer and the stable layer heights have been derived as 375 m and 900 m, respectively.

5.1.2 Aerosol spectral and size distributions

The multi-channel solar radiometer (sunphotometer) is a conventional filter-wheel based radiometer and operates at 14 narrow-band wavelengths (ranging from 0.31 μm to 1.63

μm). Aerosol optical depths (AOD) were estimated from the observations of direct solar radiation by following the procedure described earlier. The day-to-day variation in the AOD observed with different optical channels of the sunphotometer during the FFP are shown in Figure 13. It is clear that the AODs are greater at smaller wavelengths and smaller at longer wavelengths as expected, suggesting abundant fine particle concentration. In addition, AODs almost at all wavelengths show increase with time, but with different slopes, which is considered to be caused by different generation mechanisms associated with aerosol particles and prevailing meteorological conditions over the experimental station. This feature is clearly seen in the AOD variations at smaller wavelengths.

Moreover, data archived with the sunphotometer on individual experimental days are grouped into forenoon (FN) and afternoon (AN) with respect to the local noon (time at which the air mass is minimum). Corresponding FN and AN optical depths are examined separately from the full-day (FD) optical depths computed from the observations of the whole day. The

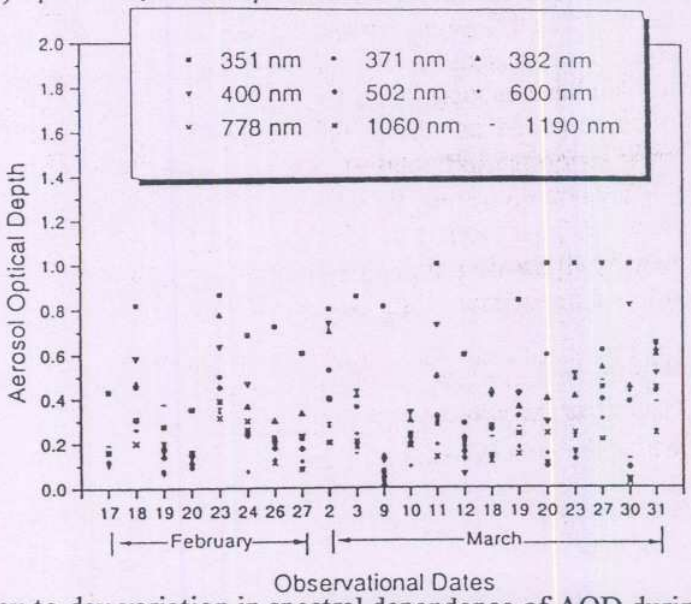

Figure 13 : Day-to-day variation in spectral dependence of AOD during FFP 98

columnar aerosol size distributions (ASD) have been inverted from the spectral variation of AOD by following the constrained linear inversion scheme discussed earlier. The wavelength

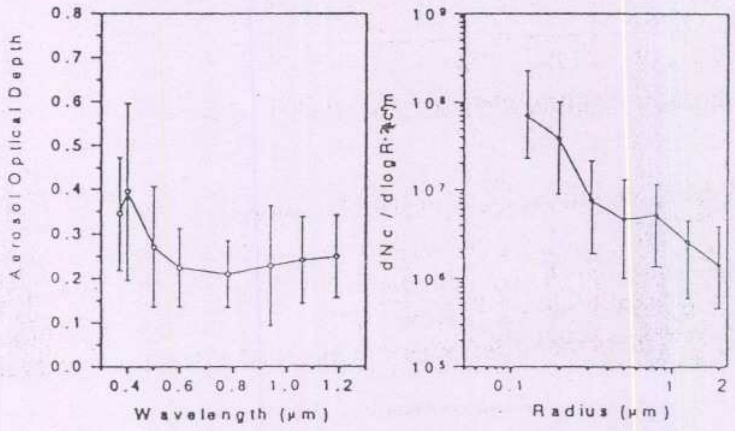

Figure 14 : Spectral variation of mean AOD and corresponding size distribution from MSR

dependence of AOD and corresponding ASDs derived from the sunphotometer for the FD period is given in Figure 14. It is found that the AN AODs are higher than the FN AODs and contribute more to the FD AODs. Moreover, the spectral dependence of plot of FD AOD show maximum value at 0.4 μm wavelength. The corresponding FD ASD exhibit bimodal distribution with a primary mode at 0.1-0.2 μm followed by a secondary mode at ~ 0.8 μm.

The data archived with the HSRR in the 04.-0.7 μm wavelength region are also examined for aerosol optical depth and physical properties. Figure 15 depict spectral distribution and associated ASDs for the FD data set. As in the case of sunphotometer, the

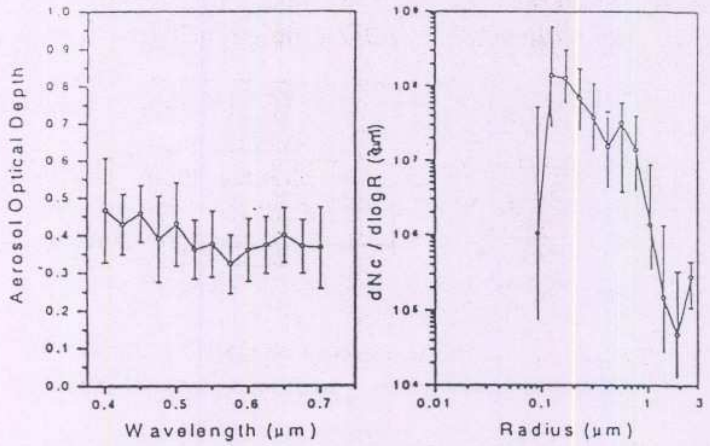

Figure 15: Mean spectral variation of AOD and corresponding size distribution from HSRR

HSRR data also show higher concentration of smaller particles during the FN period while the concentration of larger particles in the secondary mode of the size spectrum during the AN period is not clearly seen. This may be because of the difference in the range of scanning wavelengths covered by both radiometers.

5.2 Intensive field phase (IFP)

5.2.1 Vertical distributions of aerosol concentration

Vertical profiles of aerosol number density (cm^{-3}) in the altitude range 20-6900 m at 48 height intervals observed on 55 days during the three-month period of Jan - Mar 1999 have been used in the analysis. Surface meteorological parameters like the day's maximum temperature (T_{max}), minimum temperature (T_{min}) and relative humidity have been collected from IMD, Pune to examine their possible influence on the aerosol distributions over the location. Figure 16 shows the lidar-derived average vertical profile of aerosol concentration for the above three- month period of 1999. For convenience, the profile has been plotted from the minimum altitude of 100 m, instead of from 20 m as the concentrations at the lower altitudes are comparatively very high. On an average, aerosol concentration varied from 11.19 X 10^3 cm^{-3} at 20 m altitude to 0.05 X 10^3 cm^{-3} at 6900 m. The horizontal bars at each altitude in the figure show the standard deviation in concentration over the three-month period of observation. Normalized concentration gradient (NCG) profiles have been obtained for all the 55 concentration profiles to derive the Nocturnal Boundary Layer (NBL) /mixed layer and stable layer heights. The average NCG profile is also shown in Figure 16. Here it can be seen that positive concentration gradients indicative of stable layers are found to be existing at altitudes around 500 m and above.

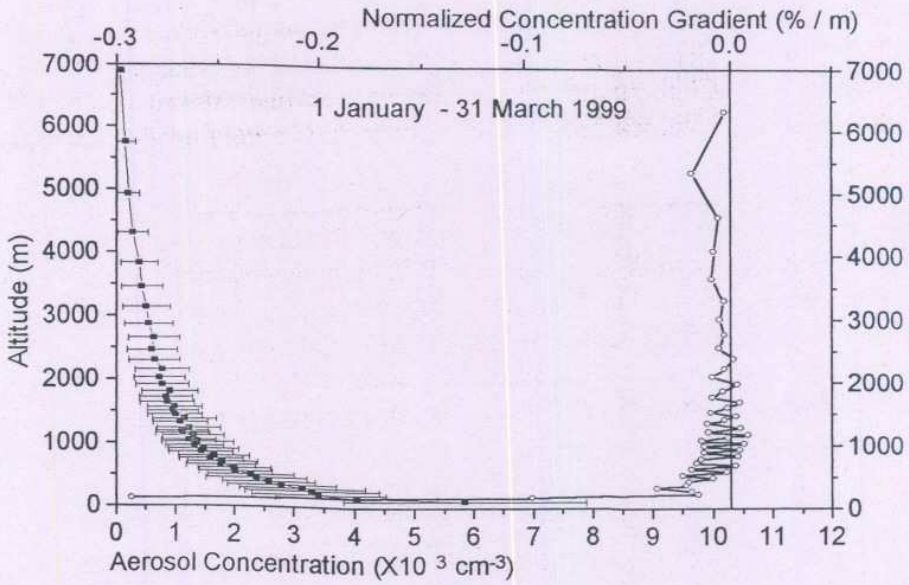

Figure 16 : Average vertical profiles of aerosol concentration and corresponding norma concentration gradient for the three-month period of 1999

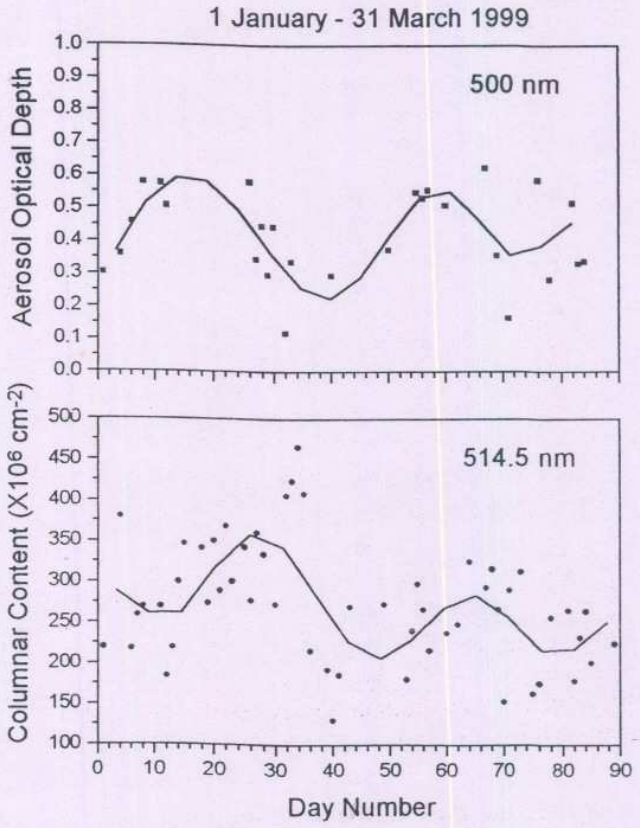

Figure 17 : Day-to-day variations in radiometer-derived aerosol optical depth at 500 nm lidar-derived aerosol columnar content at 514.5 nm

Monthly mean vertical profiles of aerosol concentration separately for January, February and March of 1999 have been obtained and observed that concentrations are relatively higher at almost all altitudes above 200 m during the month of January compared to the other two months. There also exists a vertical fine structure in the concentration profile of January whereas the profiles of February and March show a smooth altitude variation.

Time variations in lidar-derived aerosol columnar content have been compared with the radiometer-derived (the detailed results of which have been reported elsewhere in this issue) aerosol optical depth. Figure 17 shows the day-to-day variations in radiometer-derived aerosol optical depth at 500 nm and lidar-derived aerosol columnar content at 514.5 nm. A higher order polynomial fit has also been drawn and shown in the figure for the two data sets. It is observed that two prominent maxima are seen simultaneously in both the data sets, one during the month of January and the other during the month of March with a minimum during February. However, on a closer examination one can see that the lidar-derived aerosol columnar content variations seem to be lagging columnar aerosol optical depth by about 10 days.

5.2.2 Mean aerosol optical depth and size distribution

The behaviour of aerosol optical depth and corresponding size distribution, averaged over the entire IFP, are examined in Figure 18. Though the optical depth ranges are almost same, the wavelength dependence of optical depth is different for fullday, forenoon and afternoon periods. The significant changes observed in the fullday, forenoon and afternoon size distributions could be due to these differences.

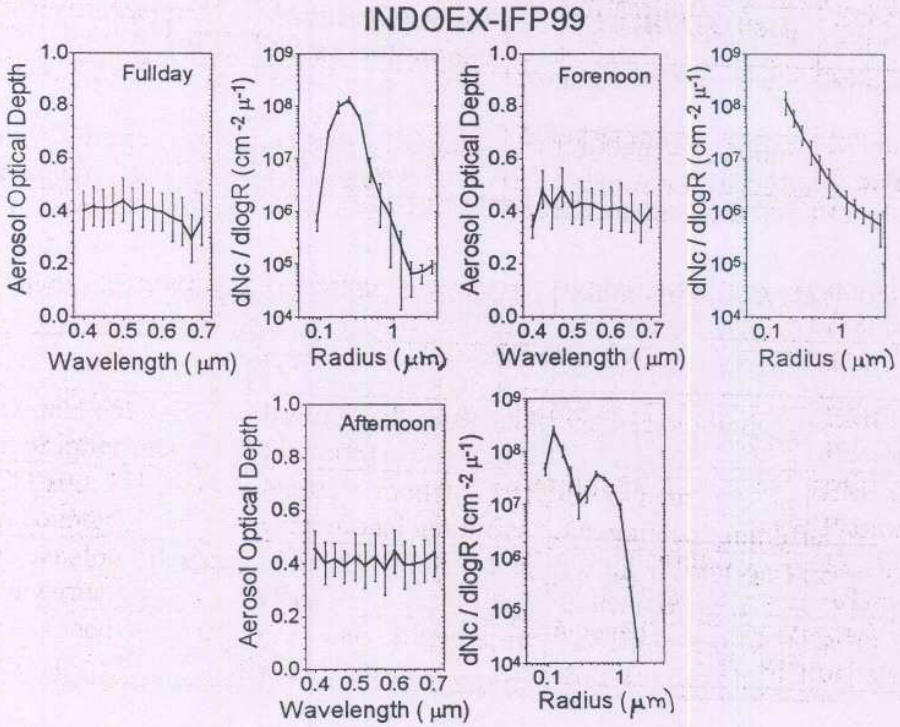

Figure 18 : Spectral dependence of aerosol optical depth and corresponding size distribution from HSRR during the entire IFP period

The size distribution showed monomodal during fullday, power law type during the forenoon and bimodal during the afternoon period.

The AOD data collected, at different wavelengths of the radiometers, on individual experimental days during January - March 1999 are averaged to obtain monthly mean spectral distributions. Columnar aerosol size distribution for each month is obtained by inverting the monthly mean multi-spectral optical depth data. The spectral variation of AOD and corresponding size distribution, averaged over the entire IFP, are shown plotted in Figure 19. On close examination, these plots mainly reveal that the AOD decreases exponentially with increase in wavelength which is in accordance with the Mie theory of aerosol scattering. It is also noticed that although these spectral and size distributions are significantly different on some experimental days during the IFP, the observed monthly and IFP mean variations show almost similar behavior, which may be due to the time averaging of changes in local aerosol sources / meteorological parameters.

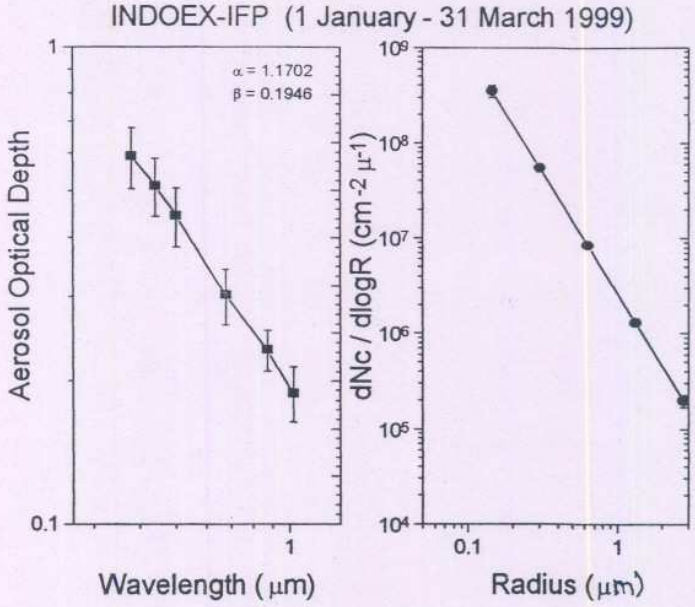

Figure 19 : Spectral variation aerosol optical depth during IFP (January - March 1999). Vertical bars represent standard errors

5.2.3 Association between AOD, precipitable water content and ozone

The day-to-day variations in columnar AOD at 0.38 μm, 0.5 μm and 1.02 μm (as representative of beginning, middle and ending portions of the size spectrum considered in the experiment) wavelengths, precipitable water content and ozone during the entire period of IFP99 were examined. A fairly good agreement is noticed between the AOD variations at 0.38 μm, columnar precipitable water content and ozone. Such a plot depicting the significant correlation between the AOD and columnar precipitable water content variations with a coefficient of 0.69 is shown in Figure 20(a). Similar plot between the variations in AOD and total column ozone which showed negative correlation coefficient of 0.40 is shown in Figure 20(b). The correlation coefficients for the variations in AOD at 0.5 μm with those in total columnar precipitable water content (0.69) and ozone (0.026), and the variations in AOD at 1.02 μm with those in total columnar precipitable water content (0.29) and ozone (0.09) are found to be smaller and hence they are not shown in the figure. These depths, on an average, are higher as compared to those (Devara et al., 1999b) observed during the FFP98. In addition, IFP99 aerosol size spectra exhibit greater concentrations of accumulation- and coarse-mode particles but with almost similar width as those of FFP98. The synchronous observations carried out using the lidar and HSRR at this experimental site

also showed similar results (Ernest Raj et al., 2000; Maheskumar et al., 2000). These differences are attributed mainly due to frequent occurrence of close-to-surface inversion and resultant haze formation and trapping of human-induced aerosols in proximity to the experimental station. It is evident from the Figure 20(a) that the variations in optical depth and water content follow each other implying increase in aerosol extinction with increase in water content and vice versa. This relationship can be explained on the basis of growth of aerosol particles which are insensitive to the wavelength of observation before being sensed

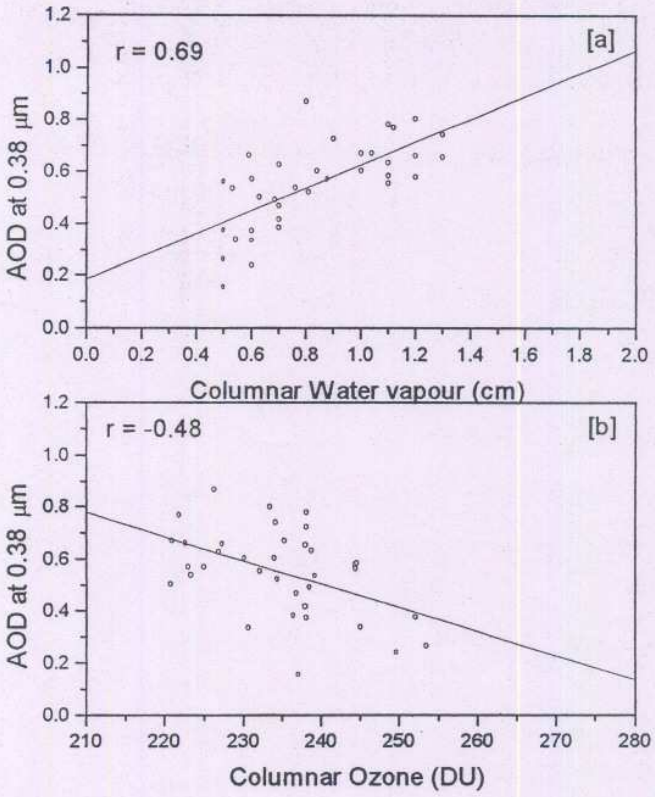

Figure 20 : Day-to-day variations in columnar aerosol optical depth, precipitable water content and ozone during the IFP99

and also through further growth of particles that are already existing at the time of observation. The relationship between the day-to-day variations in the AOD at 0.38 µm and ozone is shown in Figure 20(b). Such a relationship which resembles that of heterogeneous chemical effect has also been observed in our earlier studies (Devara et al., 1999c). This can be explained on the basis of increase in aerosol surface area and resultant reduction in ozone amount. This is possible because aerosols also act as idealized surfaces or catalysts for gas phase reactions. However, in the present study, this type of relationship between AOD and ozone is observed only during certain meteorological conditions and this phenomenon, especially over tropics, is not much clear. Hence, it needs further study. Since regular radiometric observations of AOD, water content and ozone are continuing at Pune, it is hoped that this feedback process between aerosol and ozone could be made more clear with large number of datasets.

5.2.4 Contribution of boundary layer AOD to total

Figure 21 [a&b] depicts daily variation of L_{AOD} computed from the lidar-derived aerosol column content estimated in the air layer between 0 and 1100 m (representing the boundary layer over the experimental station). Figure 21[a] depicts daily variations of lidar-derived boundary layer aerosol optical depth (L_{AOD}) and radiometer derived total column optical depth (R_{AOD}) computed at the same wavelength of 0.5 μm. Also shown in the figure

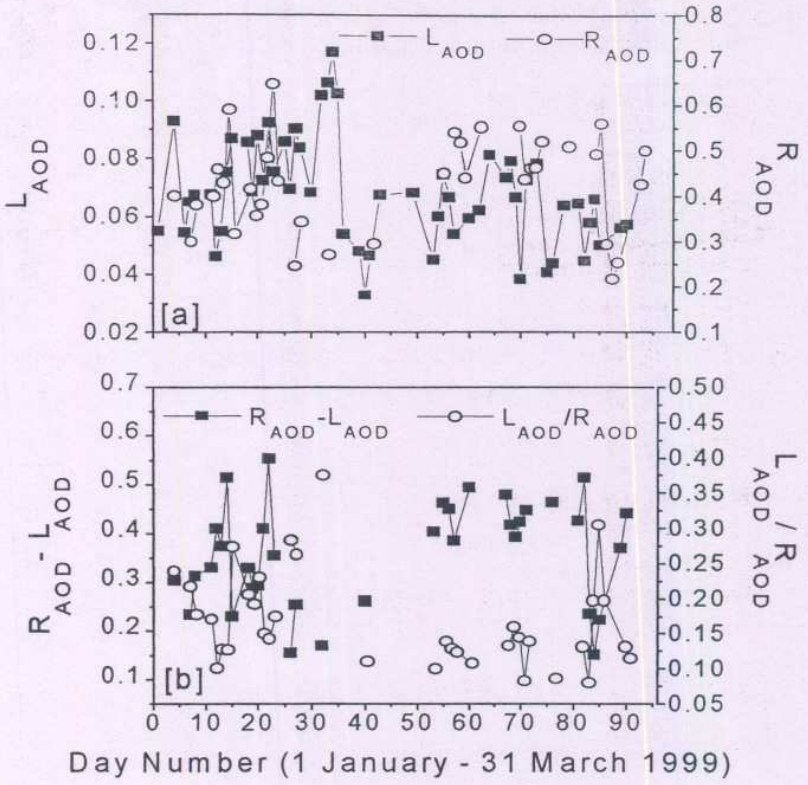

Figure 21 : Variations in boundary layer optical depth and total column optical depth and their relative contributions observed during 1 January through 31 March 1999

(panel b) are the difference and ratio between these optical depths which (represent fairly the tropospheric optical depth) and contribution of boundary layer aerosols (indicator of surface-generated aerosols and precursor gases due to human activities) to the total column optical depth. The figure clearly shows close correspondence between the variations in L_{AOD} and R_{AOD} which reveals that the trend of variation in AOD is not-confined only to the boundary layer but also to the layer aloft up to the stratosphere. The contribution of L_{AOD} to R_{AOD} is found to be about 25% is quite high in January as compared to later period of the experiment.

5.3 Marine aerosol characterization

As a part of the INDOEX-IFP, the multi-channel solar radiometer (sunphotometer) of the Institute has been operated over the Oceans. The results obtained from the aerosol extinction data collected over Oceans are discussed below.

A scientific cruise (# SK141) was planned, onboard ORV Sagar Kanya, as part of IFP of INDOEX (January 20 – March 12, 1999), to study aerosol characteristics, among others, in

and around ITCZ and also in pure and pristine Oceanic environment. The cruise covered the latitude belt between 17^0N and 20^0S and longitude belt between 71^0 E and 59^0 E of the Indian Ocean and Arabian Sea regions in a total period of 52 days. The cruise started from Goa on

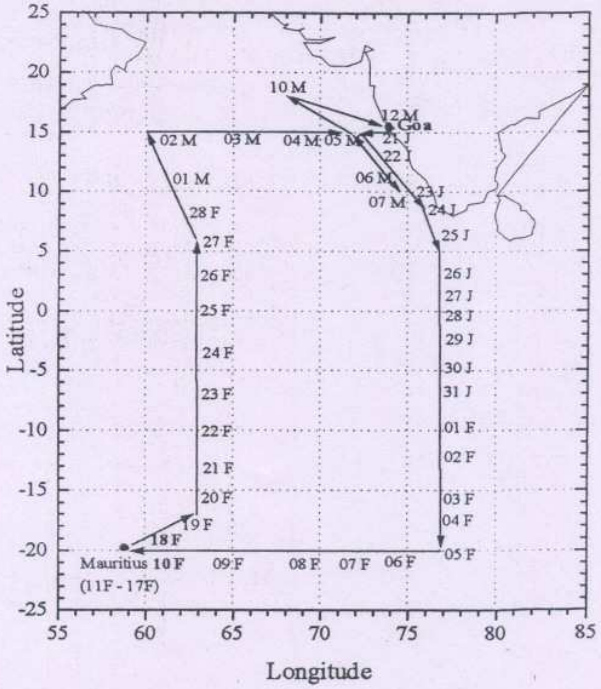

Figure 22 : The cruise track of ORV Sagar Kanya during INDOEX IFP along with wind vector

January 20, 1999 and ended on March 12, 1999 after having a port call at Port-Louis, Mauritius (February 11 - 17, 1999). Figure 22 shows the cruise track of ORV Sagar Kanya during IFP. Experiments have been carried out onboard, using multi-channel solar radiometer to study spectral - temporal aerosol characteristics. The instrument was mounted in front of the bridge of the ship, which is about 10 m above the sea surface, where the effects due to pitch and rolling of the ship are minimum. This arrangement also facilitated to minimise the contamination from chimney of the ship and sea spray during rough sea conditions.

The day-to-day variation in AOD observed with different optical channels is shown in Figure 23. AODs show greater values close to Indian sub-continent and then decrease significantly as the ship moved into pristine oceanic environment. It is clear from this figure that AODs for longer wavelengths show greater values implying the abundance of larger particle concentration close to the Indian coast during forward leg as compared to that of return leg of the cruise.

The spatial distribution of AOD at 0.502 μm during the cruise period is presented in Figure 24. A suitable software package has been used for contouring the latitude longitude variation of AOD depicted in the figure. Pockets of enhanced AOD can be noticed between latitudes 5^0 and 17^0 N and longitudes 59^0 and 68^0 E. Similar pockets but with lesser

magnitude of AOD are also noticed along the Indian coast. The wind field pattern at different pressure levels may explain the causative mechanism for these observed higher AOD. Considering the position of the ITCZ around 5^0 S during the period of the cruise,

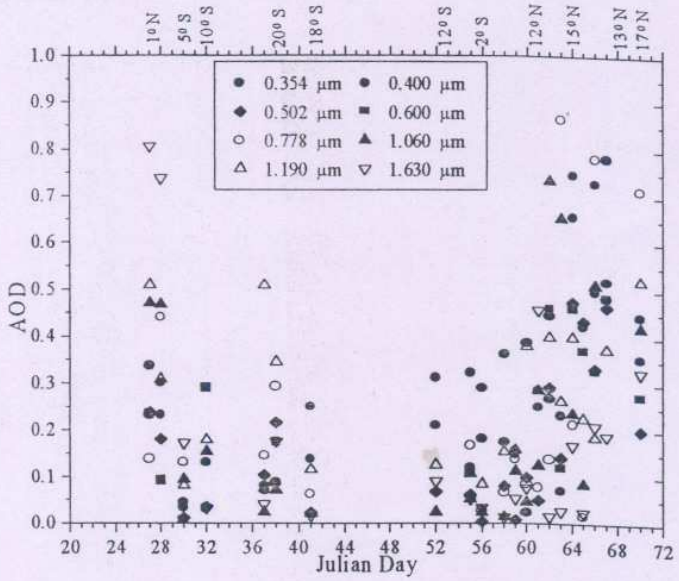

Figure 23 : Day-to-day variation of AOD for different optical channels

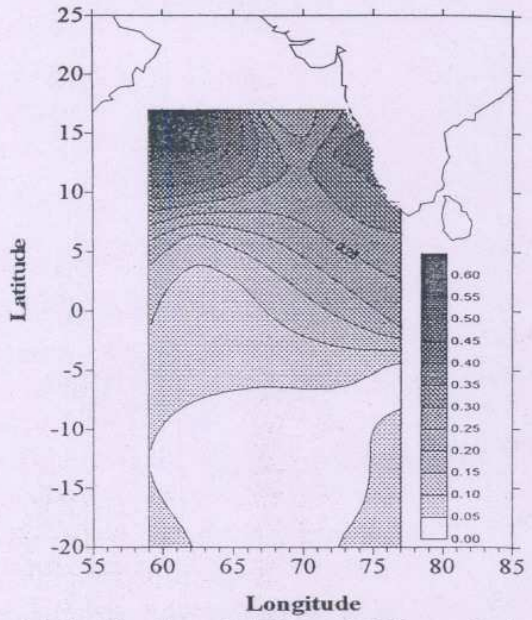

Figure 24 : Spatial distribution of AOD at 0.502 µm during the cruise period

the AODs around ITCZ are examined. Higher value of AOD north of ITCZ with significant latitudinal gradient compared to that of south of ITCZ is clearly evident from this figure.

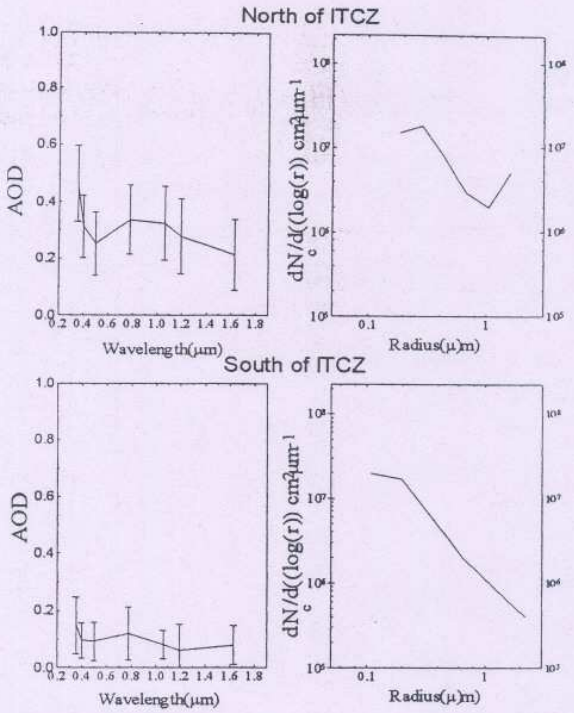

Figure 25 : Spectral dependence of mean AOD and corresponding aerosol size distribution for north (top panels) and south (bottom panels) of ITCZ

In order to study the spectral and size distribution of aerosols on either side of the position of ITCZ, the entire AOD data are divided into two groups representing north and south of ITCZ. Figure 25 shows the spectral dependence of mean AODs and corresponding particle size distributions for north (top panels) and south (bottom panels) of ITCZ. It is evident from this figure that the AOD values are significantly higher in the region north of ITCZ as compared to that of south of ITCZ. Aerosol size distributions corresponding to north and south of ITCZ (right side panels of Figure 25) show mono modal distribution for both the regions with size ranging from 0.1 to 2.2 μm. However, the aerosol size distribution corresponding to north of ITCZ shows a tendency to exhibit secondary peak towards coarse particle size > 1 μm.

5.4 Inter-comparison experiments

5.4.1 Over different environments

The MSR used in the present study was also operated at Thiruvananthapuram, a south-west coastal station, during the inter-comparison of several instruments conducted during 5-10 January 1998 prior to the INDOEX-FFP 98 programme. AODs and ASDs were obtained from the data collected on 6 January 1998. These parameters were examined in contrast to such information available at Pune with the same instrument just after a week. The spectral variations in AOD and derived ASDs over coastal Thiruvananthapuram and urban Pune are compared in Figure 26. Although the AODs show similar variation with wavelength at both stations, they are higher over Pune as expected. Also, the ASD shows bimodal distribution with a primary peak around 0.1μm at both stations. The concentrations of course-mode particles which constitute the secondary peak in the size spectrum, however are greater at Thiruvananthapuram than at Pune. This is in accordance with the properties of

aerosol particles present over the experimental stations. Although the particle concentration is low, the ASD over Pune shows broader secondary peak, indicating contributions from different sources at the experimental station and higher concentrations of accumulation-mode particles.

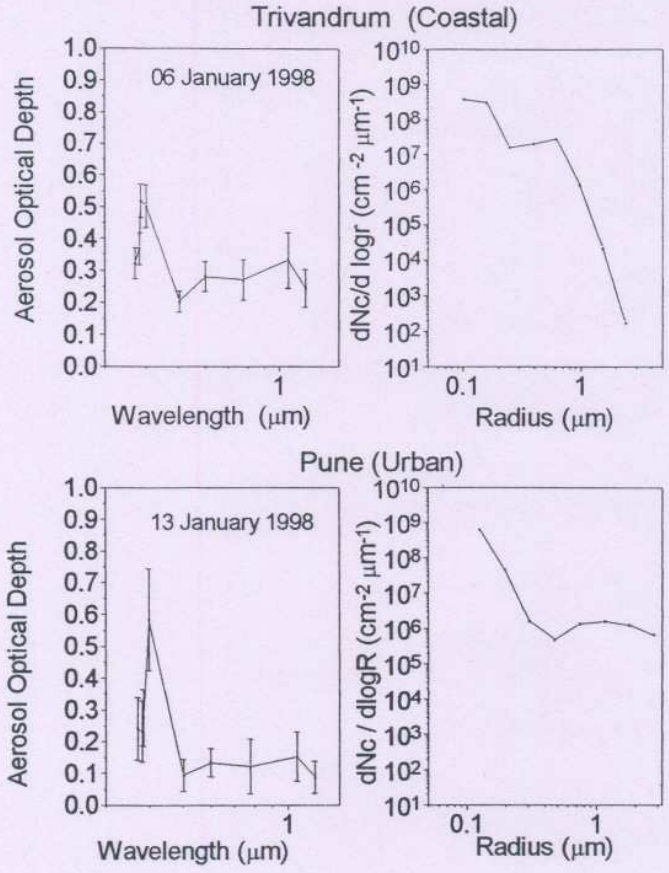

Figure 26 : Comparison of AOD and ASD over Pune and Trivandrum

5.4.2 Variations in aerosol loading

Figure 27 displays the daily variation in lidar-derived aerosol column content (loading) during the period of FFP, estimated for the altitude region of 50-1200 m from the corresponding aerosol number density profiles. The variation in aerosol loading show an increasing trend which may arise from meteorological conditions prevailing over the station. A polynomial regression analysis reveals an increase of about 20 per cent in the aerosol loading at the station over this short period. This increase in aerosol content is reasonable and also expected as the air mass undergoes considerable changes from winter to pre-monsoon months over Pune.

The aerosol loading in the month of January was higher during the IFP. Also there is large day-to-day variability within the three month period of observation. Aerosol loading was relatively smaller during February. It is also observed that the aerosol loading

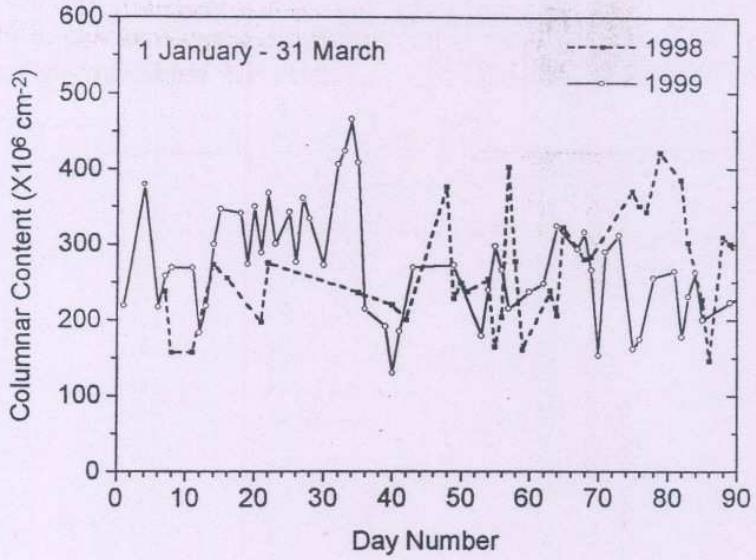

Figure 27 : Day-to-day variation in aerosol column content

was slightly higher during 1999 (IFP) than during the same period in 1998 (FFP). This increase in aerosol loading during IFP is attributed to the influence of surface meteorological parameters such as temperature range, maximum temperature and relative humidity during 1999. Table 3 shows the average aerosol column content for the three months during (January-March) 1998 and 1999. From the table it is evident that longer spells of hot and dry conditions over the observing station during 1999 might have contributed to the observed higher aerosol loading in that year.

Table 3 : Average values of lidar-derived aerosol columnar content and corresponding surface meteorological parameters

Parameter/Year	1998	1999
Aerosol columnar content (X 10^6 cm^{-2})	264.9	272.0
Day's maximum temperature (°C)	31.9	32.6
Temperature Range (°C)	18.5	19.5
Relative Humidity (%)	77.0	74.6
No. of days with temperature ≥ 35 °C	19	35

5.4.3 *Trends in AOD variation*

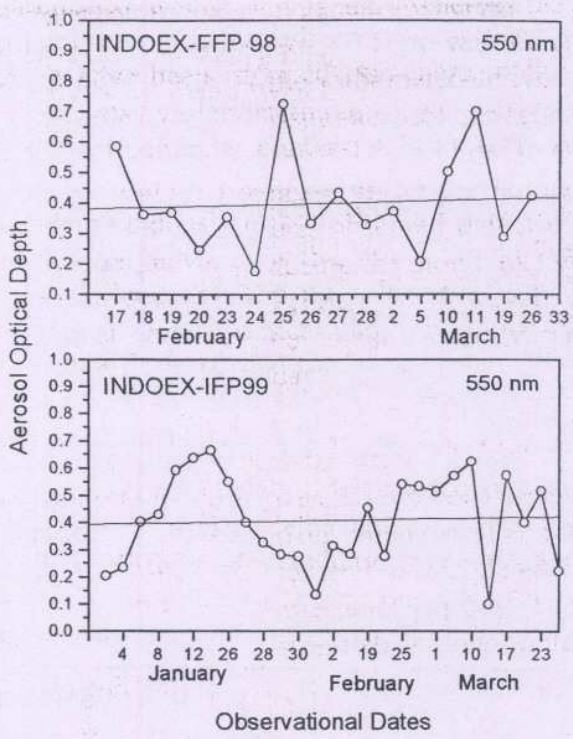

Figure 28 : Day-to-day variation in aerosol optical depth

The variations observed in the AOD at the 0.55 μm wavelength during FFP and IFP are shown in the figure 28. The polynomial fit to the data showed an increasing trend in support to the trend observed from lidar-derived aerosol loading. Hence this feature confirms the enhancement of aerosol loading over the experimental site during FFP. The linear regression fit line showed an increasing trend during the IFP period.

5.4.4 *Trend in Junge size exponent*

The wavelength exponent, α which gives an idea of the size distribution of aerosol particles have been computed from the wavelength dependence of aerosol optical depth. The day-to-day variation in α during FFP 98 and IFP 99 is shown plotted in the figure 29. The linear regression fit line to the data show an decreasing trend during the period of FFP 98 and an increasing trend during the period of IFP 99, which implies that the larger particle concentration is increasing during FFP and smaller particles concentration is more during IFP.

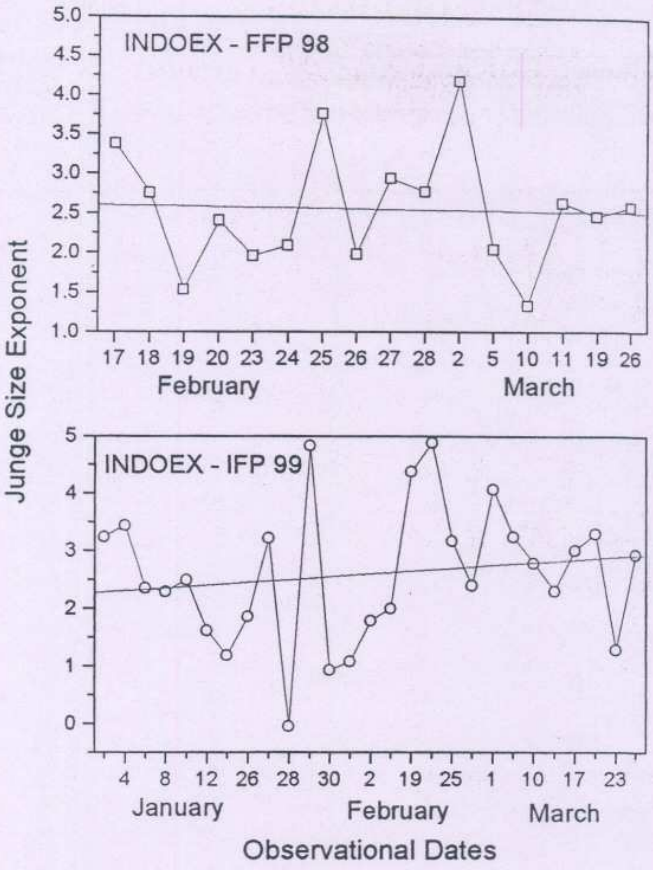

Figure 29 : Day-to-day variation in aerosol size exponent

5.4.5 Time variations in total ozone observed from ground-based and satellite data

The total column ozone which is measured by the ground-based MICROTOPS ozonometer on each day of the observation during the IFP 99 was compared with the Earth Probe satellite-based Total Ozone Mapping Spectrometer (TOMS) derived ozone for this station. Figure 30 depicts the day-to-day variation of column ozone from both ozonometer as well as from TOMS probe. The correlation coefficient was 0.88 which is statistically significant. It is interesting to note that the variations in total ozone observed by both the techniques show very good agreement.

5.4.6 Variations in ventilation coefficient

Ventilation coefficient which is a product of mixed layer height and the mean wind speed through the mixed layer has been obtained. The ventilation coefficient represents the rate at which the air within the mixed layer is transported and hence the air pollution potential over a place. The Figure 31 shows the variation of ventilation coefficient during the period from January to March in 1998 and in 1999. The ventilation coefficient variations are more closely associated with wind variations than that of mixing depth suggesting transport of

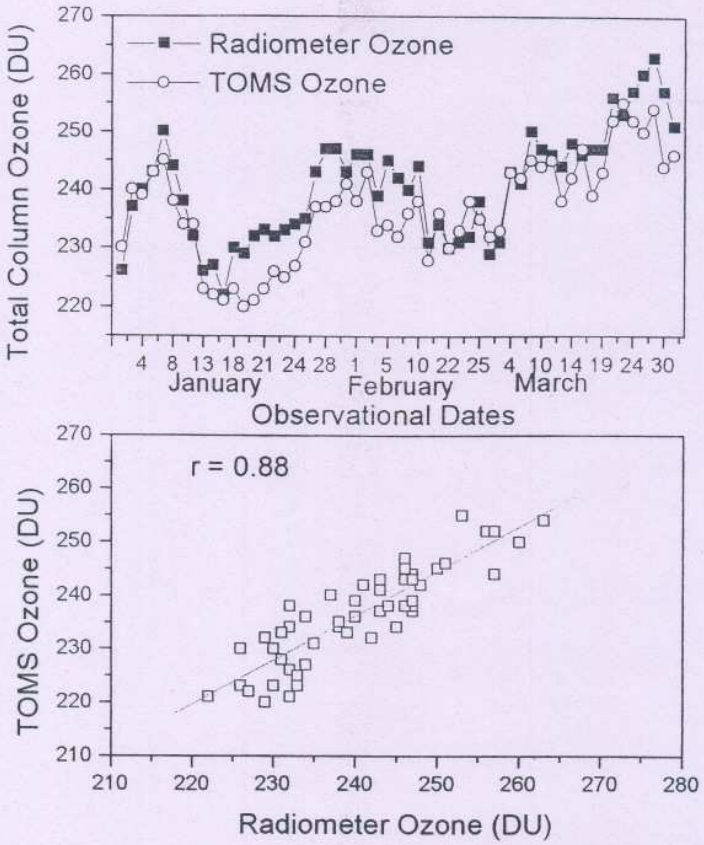

Figure 30 : Comparison between variations in total ozone observed from ground-based and space-borne probes

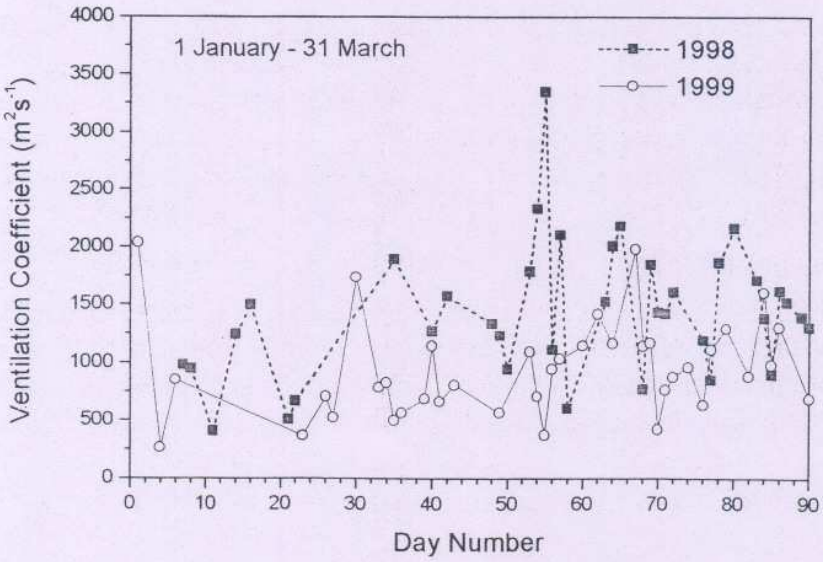

Figure 31 : Day-to-day variation in ventilation coefficient

pollutants is mainly due to wind field rather than temperature field. The average ventilation coefficient during 1998 was found to be 1613 m^2s^{-1} and the same during 1999 was about

938.35 m^2s^{-1} suggesting the air quality was poor during 1999 when compared to that during 1998.

6. Conclusions :

The study emphasizes that the information on both continental and marine aerosol properties is essential for a detailed understanding of the optical state of the atmospheric aerosols near the vicinity of the ITCZ. The main results obtained during FFP 98 and IFP 99 are summarized below :

INDOEX-FFP 98

The lidar derived vertical distributions of aerosol characteristics indicate :

- Variation in average aerosol concentrations from 9000 to 74 cm^{-3} between the altitudes 50 m and 6.88 km.
- Large negative height gradients in aerosol concentrations up to about 200 m and thereafter exponential decay with increase in altitude.
- Increasing trend (~ 20 %) in daily variation of aerosol column content which is attributed to the changes in the air mass characteristics from winter to pre-monsoon .

The radiometer observed AOD and size distribution reveal :

- The radiometer-derived full day optical depths range between 0.21 and 0.47 and the corresponding the size distribution exhibited bimodal type with accumulation-mode around 0.2 μm and coarse-mode around 1.0 μm.
- Increasing trend in daily variation of aerosol optical depth at 550 nm.

INDOEX-IFP 99 :

The lidar observations exhibited :

- Variation in aerosol concentrations from 11,190 to 50 cm^{-3} between the altitudes 50 m and 6.88 km which is larger as compared to that observed to that observed during FFP.
- Greater aerosol concentration almost at all altitudes above 200 m, during January as compared to February and March.
- Higher aerosol column content during IFP 99 (272 x 10^6 cm^{-2}) in the 50-1100 m altitude range as compared to that (265 x 10^6 cm^{-2}) observed during the same three month period which includes FFP 98.

The HSRR observed AOD and size distribution exhibited :

- Greater optical depths (more than double) on hazy days as compared to clear stable days. The optical depths varied between 0.1 to 0.8 which is compared to that during FFP 98.
- Positive correlation between optical depths and water vapour during the high humid conditions and negative correlation between optical depths and ozone during the low temperature conditions.
- Power-law type and bimodal type size distributions.

The MSR observed aerosol optical depth and size distribution during the IFP 99 cruise showed :

- ❖ Higher optical depths close to the Indian coast and lower in the pristine Ocean.
- ❖ Almost similar magnitudes of land and marine optical depths, on certain observational days, close to Indian sub-continent and adjoining areas suggesting advection of continental air mass to marine regions.
- ❖ Higher values of optical depths north of equator as compared to that to south.
- ❖ Greater values of optical depths at 502 nm wavelength north of ITCZ with significant latitudinal gradient as compared to that of south of ITCZ.

The inter-comparison of the results obtained during the two phases of INDOEX indicates :

- Higher optical depths and lower concentration of coarse-mode aerosol particles over Pune (urban station) in contrast to Thiruvananthapuram (coastal station) where the coarse-mode particles dominated the size spectrum
- Higher aerosol column content during IFP 99 when compared to that during the same period in FFP 98, which is attributed to more number of hot and dry days during 1999
- Increasing trend in AOD at 550 nm observed from HSRR during FFP and also during IFP
- Junge size exponent showed decreasing trend during FFP 98 (more number of larger particles) and increasing trend during IFP 99 (more number of smaller particles)
- Total column ozone derived from MICROTOPS ozonometer and from TOMS probe exhibited a good correlation of about 0.88 during the IFP 99.
- The ventilation coefficient derived from the lidar observed to be about 1613 m^2s^{-1} during 1998 and was about 938.35 m^2s^{-1} during 1999 indicating the quality of air during 1999 was poor when compared to that during 1998.

Acknowledgements : We gratefully acknowledge the encouragement by Dr. G.B. Pant, Director, IITM, and Dr. A.P. Mitra, Chief Scientist, INDOEX-India Program. The work reported here is a part of the INDOEX-India program supported by Department of Space (DOS), Council of Scientific and Industrial Research (CSIR), Department of Ocean Development (DOD), Department of Science and Technology (DST) and Department of Electronics (DOE), with DOS as the nodal agency. Direct funding has been provided by DOS and CSIR and in kind, support is being provided by the other agencies. The experiments performed onboard ORV Sagar Kanya were possible essentially because of the support in terms of providing the ship and necessary help by the Antarctic Study Centre of DOD. In this context, efforts put in by the National Institute of Oceanography (NIO) are also thankfully acknowledged. The meteorological data used in the studies reported here have been provided by the India Meteorological Department (IMD), Pune. One of the authors (RSM) would like to thank the INDOEX-India Program Office for the award of Research Associateship. Thanks are also due to referees for their useful comments / suggestions.

References

Charlson, R.J., Schwartz, S.E., Hales, J.M., Cess, R.D., Coakley Jr., J.A., Hansen, J.E., and Hofmann D.J., 1992 : Climate forcing by anthropogenic aerosols, *Science*, **255**, 423-430.

Devara, P.C.S. and Raj, P.E. 1991: Study of atmospheric aerosols in a terrain-induced nocturnal boundary layer using bistatic lidar, *Atmos. Environ.*, **25A**, 655-690.

Devara, P.C.S. and Raj, P.E., 1987 : A bistatic lidar for aerosol studies, *J. Inst. Electron. Telecommun. Engrs. Tech. Rev.*, **4**, 412-415.

Devara, P.C.S. and Raj, P.E., 1989 : Remote sounding of aerosols in the lower atmosphere using a bistatic, CW Helium-Neon lidar, *J. Aerosol Sci.*, **20**, 37-44.

Devara, P.C.S. and Raj, P.E., 1993 : Lidar measurements of aerosols in the tropical atmosphere, *Adv. Atmos. Sci.*, **10**, 365-378.

Devara, P.C.S., Raj, P.E., Sharma, S. and Pandithurai, G., 1994 : Lidar-observed long-term variations in urban aerosol characteristics and their connection with meteorological parameters, *Intl. J. Climatology*, **14**, 581-591.

Devara, P.C.S., Ernest Raj, P., Maheskumar, R.S., Dani, K.K. and Pandithurai, G. 1999 : 'Ground-based lidar studies aerosols and boundary layer characteristics during INDOEX First Field Phase', *Current Science* , **76**, 973-976.

Devara, P.C.S., Maheskumar, R.S. and Pandithurai, G., 1999 : On the aerosol-ozone relationship at a tropical urban station in India. *J. Atmos. Sci.* (Submitted).

Devara, P.C.S., Maheskumar, R.S., Ernest raj, P., Dani K.K. and Sonbawne, S.M., 2001 : Some Features of Columnar Aerosol Optical Depth, Ozone and Water Vapor Observed Over Land During the INDOEX-IFP99, *Meteorologische Zeitschrift*, **10**, 123-130.

Devara, P.C.S., Maheskumar, R.S., Ernest Raj, P., Pandithurai, G. and Dani, K.K. 1999 : 'Correlative measurements of aerosol optical depth and size distribution around INDOEX-FFP from multi-spectral solar radiometry', *Current Science*, **76**, 977-980.

Devara, P.C.S., Raj, P.E., Pandithurai, G. and Sharma, S., 1995 : A high spectral resolution radiometer for atmospheric monitoring, *J. Instrum. Soc. India*, 25: 142-154.

Devara, P.C.S., Raj, P.E., Sharma, S and Pandithurai, G., 1995 : Real-time monitoring of atmospheric aerosols using a computer-controlled lidar, *Atmos. Environ.*, **29**, 2205-2215.

Endlich, R.M., Ludwig, F.L. and Uthe, E.E., 1979 : An automatic method for determining the mixing depth from lidar observations, *Atmos. Environ.*, **13**, 1051-1056.

Ernest Raj, P. and Devara, P.C.S., 1989 : Some results of lidar aerosol measurements and their relationship with meteorological parameters, *Atmos. Environ.*, **23**, 831-838.

Ernest Raj, P., Devara, P.C.S., Maheskumar, R.S., Dani, K.K. and Saha, S.K. 2001 : Spatio-temporal variations in lidar-derived aerosol concentrations at Pune during INDOEX-IFP, *Curr. Sci.*, **80,** 112-114.

Jayarao, Y. and Devara, P.C.S., 2001 : Characterization of aerosols over Indian Ocean and Arabian Sea during INDOEX-IFP99 *Current Sci.*, 80, 120-122.

King, M.D., Byrne, D.M., Herman, B.M. and Reagan, J.A., 1978 : Aerosol size distributions obtained by inversion of spectral optical depth measurements, *J. Atmos. Sci.*, **35**, 2153-2167.

Kneizys, F.X., Shettle, E.P., Gallery, W.O., Chetwynd, J.H. Abreu, L.W., Selby, J.E.A., Fenn, R.W. and McClatchey, R.A., 1980. : *Atmospheric Transmittance/Radiance Computer Code LOWTRAN 5* **AFGL-TR-80-00067**, US Air Force, Environ. Res. Paper No. 697.

Krishnaraddi S. Navalli, 1968 : Forecasting and hindcasting of waves for Mangalore coastal area, M.Tech Thesis submitted to REC, Surathkal.

Maheskumar, R.S., 1999 : Atmospheric aerosol and air quality studies using lidar and *in-situ* techniques, Ph.D. Thesis, University of Pune, Pune, 200 pp.

Maheskumar, R.S., Devara, P.C.S., Ernest Raj, P., Dani K.K, 2001 : Optical characteristics of atmospheric aerosols as inferred from a high spectral resolution radiometer during the INDOEX-IFP 99, *Current Science*, **80,** 115-119.

Mitra A.P., 1999 : INDOEX (India) : Introductory note, *Current Science*, **76**, 886-889.

Ramanathan, V., Crutzen, P.J., Coakley, J., Dickerson, R., Heymsfeld, A., Kiehl, J., Kley, D., Krishnamurti, T.N., Kuettner, J., Lelieveld, J., Mitra, A.P., Prospero, J., Sedourney, R., Valero, F.P.J. and Woodbridge, E.L., 1995 : Indian Ocean Experiment (INDOEX) white paper, July C^4 Publication # 143.

Sasano, Y., Matsui, I, Shimizu, H., and Takeuchi, N., 1983 : Automatic determination of atmospheric mixed layer height in routine measurements by a laser radar, *J. Japan Soc. Air Pollut.*, **18**, 175-183.

Sasano, Y., Sigematsu, A., Shimizu, A., Takuchi, N., Okuda, M., 1982 : On the relationship between the aerosol layer height and the mixed layer height determined by laser radar and low-level radiosonde observations, *J. Meteorol. Soc.* Japan, **60**, 889-895.

I. I. T. M. RESEARCH REPORTS

- Energetic consistency of truncated models, *Asnani G.C.*, August 1971, RR-001.
- Note on the turbulent fluxes of heat and moisture in the boundary layer over the Arabian Sea, *Sinha S.*, August 1971, RR-002.
- Simulation of the spectral characteristics of the lower atmosphere by a simple electrical model and using it for prediction, *Sinha S.*, September 1971, RR-003.
- Study of potential evapo-transpiration over Andhra Pradesh, *Rakhecha P.R.*, September 1971, RR-004.
- Climatic cycles in India-1: Rainfall, *Jagannathan P. and Parthasarathy B.*, November 1971, RR-005.
- Tibetan anticyclone and tropical easterly jet, *Raghavan K.*, September 1972, RR-006.
- Theoretical study of mountain waves in Assam, *De U.S.*, February 1973, RR-007.
- Local fallout of radioactive debris from nuclear explosion in a monsoon atmosphere, *Saha K.R. and Sinha S.*, December 1972, RR-008.
- Mechanism for growth of tropical disturbances, *Asnani G.C. and Keshavamurty R.N.*, April 1973, RR-009.
- Note on "Applicability of quasi-geostrophic barotropic model in the tropics", *Asnani G.C.*, February 1973, RR-010.
- On the behaviour of the 24-hour pressure tendency oscillations on the surface of the earth, Part-I: Frequency analysis, Part-II: Spectrum analysis for tropical stations, *Misra B.M.*, December 1973, RR-011.
- On the behaviour of the 24 hour pressure tendency oscillations on the surface of the earth, Part-III : Spectrum analysis for the extra-tropical stations, *Misra B.M.*, July 1976, RR-011A.
- Dynamical parameters derived from analytical functions representing Indian monsoon flow, *Awade S.T. and Asnani G.C.*, November 1973, RR-012.
- Meridional circulation in summer monsoon of Southeast Asia, *Asnani G.C.*, November 1973, RR-014.
- Energy conversions during weak monsoon, *Keshavamurty R.N. and Awade S.T.*, August 1974, RR-015.
- Vertical motion in the Indian summer monsoon, *Awade S.T. and Keshavamurty R.N.*, August 1974, RR-016.
- Semi-annual pressure oscillation from sea level to 100mb in the northern hemisphere, *Asnani G.C. and Verma R.K.*, August 1974, RR-017.
- Suitable tables for application of gamma probability model to rainfall, *Mooley D.A.*, November 1974, RR-018.

- Annual and semi-annual thickness oscillation in thenorthern hemisphere, *Asnani G.C. and Verma R.K.*, January 1975, RR-020.

- Spherical harmonic analysis of the normal constant pressure charts in the northern hemisphere, *Awade S.T., Asnani G.C. and Keshavamurty R.N.*, May 1978, RR-021.

- Dynamical parameters derived from analytical function representing normal July zonal flow along 87.5 °E, *Awade S.T. and Asnani G.C.*, May 1978, RR-022.

- Study of trends and periodicities in the seasonal and annual rainfall of India, *Parthasarathy B. and Dhar O.N.*, July 1975, RR-023.

- Southern hemisphere influence on Indian rainfall, *Raghavan K.., Paul D.K. and Upasani P.U.*, February 1976, RR-024.

- Climatic fluctuations over Indian region - Rainfall : A review, *Parthasarathy B. and Dhar O.N.*, May 1978, RR-025.

- Annual variation of meridional flux of sensible heat, *Verma R.K. and Asnani G.C.*, December 1978, RR-026.

- Poisson distribution and years of bad monsoon over India, *Mooley D.A and Parthasarathy B.*, April 1980, RR-027.

- On accelerating the FFT of Cooley and Tukey, *Mishra S.K.*, February 1981, RR-028.

- Wind tunnel for simulation studies of the atmospheric boundary layer, *Sivaramakrishnan S.*, February 1981, RR-029.

- Hundred years of Karnataka rainfall, *Parthasarathy B. and Mooley D.A.*, March 1981, RR-030.

- Study of the anomalous thermal and wind patterns during early summer season of 1979 over the Afro-Asian region in relation to the large-scale performance of the monsoon over India, *Verma R.K. and Sikka D.R.*, March 1981, RR-031.

- Some aspects of oceanic ITCZ and its disturbances during the onset and established phase of summer monsoon studied with Monex-79 data, *Sikka D.R., Paul D.K. and Singh S.V.*, March 1981, RR- 032.

- Modification of Palmer drought index, *Bhalme H.N. and Mooley D.A.*, March 1981, RR-033.

- Meteorological rocket payload for Menaka-II/Rohini 200 and its developmental details, *Vernekar K.G. and Brij Mohan*, April 1981, RR-034.

- Harmonic analysis of normal pentad rainfall of Indian stations, *Anathakrishnan R. and Pathan J.M.*, October 1981, RR-035.

- Pentad rainfall charts and space-time variations of rainfall over India and the adjoining areas, *Anathakrishnan R. and Pathan J.M.*, November 1981, RR-036.

- Dynamic effects of orography on the large scale motion of the atmosphere Part I : Zonal flow and elliptic barrier with maximum height of one km., *Bavadekar S.N. and Khaladkar R.M.*, January 1983, RR-037.

- Limited area five level primitive equation model, *Singh S.S.*, February 1983, RR-038.
- Developmental details of vortex and other aircraft thermometers, *Vernekar K.G., Brij Mohan and Srivastava S.*, November 1983, RR-039.
- Note on the preliminary results of integration of a five level P.E. model with westerly wind and low orography, *Bavadekar S.N., Khaladkar R.M., Bandyopadhyay A. and Seetaramayya P.*, November 1983, RR-040.
- Long-term variability of summer monsoon and climatic change, *Verma R.K., Subramaniam K. and Dugam S.S.*, December 1984, RR-041.
- Project report on multidimensional initialization for NWP models, *Sinha S.*, February 1989, RR-042.
- Numerical experiments with inclusion of orography in five level P.E. Model in pressure-coordinates for interhemispheric region, *Bavadekar S.N. and Khaladkar R.M.*, March 1989, RR-043.
- Application of a quasi-lagrangian regional model for monsoon prediction, *Singh S.S. and Bandyopadhyay A.*, July 1990, RR-044.
- High resolution UV-visible spectrometer for atmospheric studies, *Bose S., Trimbake H.N., Londhe A.L. and Jadhav D.B.*, January 1991, RR-045.
- Fortran-77algorithm for cubic spline interpolation for regular and irregular grids, *Tandon M.K.*, November 1991, RR-046.
- Fortran algorithm for 2-dimensional harmonic analysis, *Tandon M.K.*, November 1991, RR- 047.
- 500 hPa ridge and Indian summer monsoon rainfall : A detailed diagnostic study, *Krishna Kumar K., Rupa Kumar K. and Pant G.B.*, November 1991, RR-048.
- Documentation of the regional six level primitive equation model, *Singh S.S. and Vaidya S.S.*, February 1992, RR-049.
- Utilisation of magnetic tapes on ND-560 computer system, *Kripalani R.H. and Athale S.U.*, July 1992, RR-050.
- Spatial patterns of Indian summer monsoon rainfall for the period 1871-1990, *Kripalani R.H., Kulkarni A.A., Panchawagh N.V. and Singh S.V.*, August 1992, RR-051.
- FORTRAN algorithm for divergent and rotational wind fields, *Tandon M.K.*, November 1992, RR-052.
- Construction and analysis of all-India summer monsoon rainfall series for the longest instrumental period: 1813-1991, *Sontakke N.A., Pant G.B. and Singh N.*, October 1992, RR-053.
- Some aspects of solar radiation, *Tandon M.K.*, February 1993, RR-054.
- Design of a stepper motor driver circuit for use in the moving platform, *Dharmaraj T. and Vernekar K.G.*, July 1993, RR-055.

- Experimental set-up to estimate the heat budget near the land surface interface, *Vernekar K.G., Saxena S., Pillai J.S., Murthy B.S., Dharmaraj T. and Brij Mohan*, July 1993, RR-056.

- Identification of self-organized criticality in atmospheric total ozone variability, *Selvam A.M. and Radhamani M.*, July 1993, RR-057.

- Deterministic chaos and numerical weather prediction, *Selvam A.M.*, February 1994, RR-058.

- Evaluation of a limited area model forecasts, *Singh S.S., Vaidya S.S Bandyopadhyay A., Kulkarni A.A, Bawiskar S.M., Sanjay J., Trivedi D.K. and Iyer U.*, October 1994, RR-059.

- Signatures of a universal spectrum for atmospheric interannual variability in COADS temperature time series, *Selvam A.M., Joshi R.R. and Vijayakumar R.*, October 1994, RR-060.

- Identification of self-organized criticality in the interannual veriability of global surface temperature, *Selvam A.M. and Radhamani M.*, October 1994, RR-061.

- Identification of a universal spectrum for nonlinear veriability of solar-geophysical parameters, *Selvam A.M., Kulkarni M.K., Pethkar J.S. and Vijayakumar R.*, October 1994, RR-062.

- Universal spectrum for fluxes of energetic charged particles from the earth's magnetosphere, *Selvam A.M. and Radhamani M.*, June 1995, RR-063.

- Estimation of nonlinear kinetic energy exchanges into individual triad interactions in the frequency domain by use of the cross-spectral technique, *Chakraborty D.R.*, August 1995, RR-064.

- Monthly and seasonal rainfall series for all-India homogeneous regions and meteorological subdivisions: 1871-1994, *Parthasarathy B., Munot A.A. and Kothawale D.R.*, August 1995, RR-065.

- Thermodynamics of the mixing processes in the atmospheric boundary layer over Pune during summer monsoon season, *Morwal S.B. and Parasnis S.S.*, March 1996, RR-066.

- Instrumental period rainfall series of the Indian region: A documentation, *Singh N. and Sontakke N.A.*, March 1996, RR-067.

- Some numerical experiments on roundoff-error growth in finite precision numerical computation, *Fadnavis S.*, May 1996, RR-068.

- Fractal nature of MONTBLEX time series data, *Selvam A.M. and Sapre V.V.*, May 1996, RR-069.

- Homogeneous regional summer monsoon rainfall over India: Interannual variability and teleconnections, *Parthasarathy B., Rupa Kumar K. and Munot A.A.*, May 1996, RR-070.

- Universal spectrum for sunspot number variability, *Selvam A.M. and Radhamani M.*, November 1996, RR-071.

- Development of simple reduced gravity ocean model for the study of upper north Indian ocean, *Behera S.K. and Salvekar P.S.*, November 1996, RR-072.

- Study of circadian rhythm and meteorological factors influencing acute myocardial infraction, *Selvam A.M., Sen D. and Mody S.M.S.*, April 1997, RR-073.

- Signatures of universal spectrum for atmospheric gravity waves in southern oscillation index time series, *Selvam A.M., Kulkarni M.K., Pethkar J.S. and Vijayakumar R.*, December 1997, RR-074.

- Some example of X-Y plots on Silicon Graphics, *Selvam A.M., Fadnavis S. and Gharge S.P.*, May 1998, RR-075.

- Simulation of monsoon transient disturbances in a GCM, *Ashok K., Soman M.K. and Satyan V.*,August 1998, RR-076.

- Universal spectrum for intraseasonal variability in TOGA temperature time series, *Selvam A.M., Radhamani M., Fadnavis S. and Tinmaker M.I.R.*, August 1998, RR-077.

- One dimensional model of atmospheric boundary layer, *Parasnis S.S., Kulkarni M.K., Arulraj S. and Vernekar K.G.*, February 1999, RR-078.

- Diagnostic model of the surface boundary layer - A new approach, *Sinha S.*, February 1999, RR-079.

- Computation of thermal properties of surface soil from energy balance equation using force - restore method, *Sinha S.*, February 1999, RR-080.

- Fractal nature of TOGA temperature time series, *Selvam A.M. and Sapre V.V.*, February 1999, RR-081.

- Evolution of convective boundary layer over the Deccan Plateau during summer monsoon, *Parasnis S.S.*, February 1999, RR-082.

- Self-organized criticality in daily incidence of acute myocardial infarction, *Selvam A.M., Sen D., and Mody S.M.S.*, Feburary 1999, RR-083.

- Monsoon simulation of 1991 and 1994 by GCM : Sensitivity to SST distribution, *Ashrit R.G., Mandke S.K. and Soman M.K.*, March 1999, RR-084.

- Numerical investigation on wind induced interannual variability of the north Indian Ocean SST, *Behera S.K., Salvekar P.S. and Ganer D.W.*, April 1999, RR-085.

- On step mountain eta model, *Mukhopadhyay P., Vaidya S.S., Sanjay J. and Singh S.S.*, October 1999, RR-086.

- Land surface processes experiment in the Sabarmati river basin: an overview and early results, *Vernekar K.G., Sinha S., Sadani L.K., Sivaramakrishnan S., Parasnis S.S., Brij Mohan, Saxena S., Dharamraj T., Pillai, J.S., Murthy B.S., Debaje, S.B., Patil, M.N. and Singh A.B.*, November 1999, RR-087.

- Reduction of AGCM systematic error by Artificial Neural Network: A new approach for dynamical seasonal prediction of Indian summer monsoon rainfall, *Sahai A.K. and Satyan V.*, December 2000, RR-088.

- Ensemble GCM simulations of the contrasting Indian summer monsoons of the 1987 and 1988, *Mujumdar M. and Krishnan R.*, February 2001, RR-089.